Marine and Petroleum Geology 148 (2023) 106018

Contents lists available at ScienceDirect

Marine and Petroleum Geology

journal homepage: www.elsevier.com/locate/marpetgeo

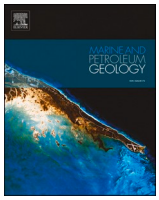

Multi-proxy reconstruction of the burial history and porosity evolution of the TOCA carbonate formation in the Lower Congo basin (South West Africa)

Boubacar Bah [a,*], Nicolas E. Beaudoin [b], Olivier Lacombe [a], Jean-Pierre Girard [b,c], Claude Gout [b,c], Nicolas Godeau [d], Pierre Deschamps [d]

[a] Sorbonne Université, Institut des Sciences de La Terre de Paris (ISTeP), CNRS-INSU, 75005, Paris, France
[b] Universite de Pau et des Pays de L'Adour, Laboratoire des Fluides Complexes et Leurs Réservoirs (LFCR), E2S UPPA, CNRS, TotalEnergies, 64000, Pau, France
[c] TotalEnergies, Centre Scientifique et Technique Jean Féger (CSTJF), 64000, Pau, France
[d] Aix Marseille Univ, CNRS, IRD, INRAE, CEREGE, Aix-en-Provence, France

A B S T R A C T

The timing of porosity destruction in reservoir rock is key for hydrocarbon exploration. This study constrains the porosity destruction of the syn-rift Barremian (130-125 Ma) TOCA Fm. from one drill core located in the Lower Congo basin (West African passive margin). We apply an unprecedented multi-proxy approach to reconstruct the absolute timing of mechanical compaction, pressure-solution and cementation as well as their relative contribution to porosity destruction. LA-ICP-MS U–Pb geochronology combined with petrological observations suggest that the main interstitial diagenetic cement C1 filling the porosity of the packstones and dated 127.4 ± 2.2 to 119.4 ± 6.4 Ma predates pressure-solution. The quantification of the cement distribution by image analysis indicates that C1 clogged ~30% of the initial porosity before the strata were buried at 400 m. We assume that the early cementation limited the effect of mechanical compaction on porosity reduction which is estimated to ~2% in the first 100 m of burial. In contrast, a first order estimate of the chemical compaction-reprecipitation can account for up to ~6% of the initial porosity destruction, as estimated by the inversion of sedimentary stylolite roughness. This technique also documents that the burial-related pressure-solution in the TOCA Fm. occurred in the 550–1750 m burial depth range corresponding to a time spanning from 117 to 95 Ma considering the burial-time model of the TOCA Fm. Our study reveals that the initial porosity of carbonates was reduced down to its current value of 4–8% within the first 35 Ma of its burial history, reaching ~10% after only 10 Ma, i.e. in the first 400–500 m of burial. This case study indicates that the fate of reservoir properties in bioclastic carbonate formations such as the TOCA Fm. may be largely controlled by early, very shallow diagenetic processes rather than subsequent deep-burial mesogenetic reactions.

1. Introduction

Carbonate sedimentary rocks are prime targets for the oil and gas industry, representing 40% of exploited plays (Ehrenberg et al., 2009), despite intrinsic reservoir properties (porosity and permeability) that are notoriously highly variable, heterogeneous and difficult to predict (Regnet et al., 2019). In addition to the large variability related to depositional environments, reservoir properties are further altered by diagenetic and structural processes including compaction, pressure-solution, fracture development and dissolution/cementation, which may take place from early burial to exhumation (Choquette and Pray, 1970; Schoeder, 1988; Moore, 1989; Tucker and Wright, 1990; Tucker, 2001; Booler and Tucker, 2002; Moore and Wade, 2013; Humphrey et al., 2019). As a consequence, the distribution of porosity and permeability, in space and in time, is a major challenge for the modelling of such reservoirs in hydrocarbon and ore exploration/exploitation, as well as greenhouse gas storage operations (Guo et al., 2006; Salem and Shedid, 2013; Wang et al., 2020). While most diagenetic studies focus on characterizing the origin and relative chronology of cements filling the porosity (e.g. Barbier et al., 2012), it is essential to be able to reconstruct the calendar and proportion of porosity destruction/enhancement during the burial and diagenetic history of the rock (Moore and Wade, 2013). Such calendar can be assessed thanks to the recent development of in situ U–Pb geochronology of carbonates (Roberts et al., 2020) which provides a way to determine the absolute age of porosity-reducing cements occurring in fractures (e.g. Beaudoin et al., 2018), or in intergranular/intercrystalline pores (e.g. Godeau et al., 2018; Li et al., 2014).

Among the other processes affecting the porosity in carbonate rocks, pressure-solution might be one of the most overlooked (Croize et al., 2013). Stylolites, i.e. serrated pressure-solution planes developed under stress (Alvarez et al., 1978; Koehn et al., 2007; Toussaint et al., 2018) are

* Corresponding author.
E-mail address: boubacar.bah@sorbonne-universite.fr (B. Bah).

https://doi.org/10.1016/j.marpetgeo.2022.106018
Received 19 July 2022; Received in revised form 17 October 2022; Accepted 7 November 2022
Available online 17 November 2022
0264-8172/© 2022 Elsevier Ltd. All rights reserved.

ubiquitous in carbonates and accommodate vertical compaction or horizontal shortening very early during burial and tectonic contraction, respectively (Andrews and Railsback, 1997; Ben-Itzhak et al., 2014; Toussaint et al., 2018; Beaudoin et al., 2020a; Gomez-Rivas et al., 2022; Xu et al., 2022). A number of recent studies (Baud et al., 2016; Koehn et al., 2016; Martin-Martin et al., 2018; Heap et al., 2014, 2018; Bruna et al., 2019; Humphrey et al., 2019) demonstrated how stylolites development and morphology impact fluid flow and alter the reservoir properties of carbonate rocks following reprecipitation of the dissolved material in adjacent pores or farther in the rock volume. It occurs that the roughness of stylolites (i.e. the difference in height between two points along a 1D track) can be used as a stress gauge (Schmittbuhl et al., 2004; Ebner et al., 2009b, 2010b; Rolland et al., 2012, 2014; Toussaint et al., 2018). This tool was developed as the so-called Stylolite Roughness Inversion Technique (SRIT, Beaudoin and Lacombe, 2018) and has been successfully applied to a number of geological problems (Renard et al., 2004; Schmittbuhl et al., 2004; Koehn et al., 2007, 2012; Ebner et al., 2010a, 2010b; Rolland et al., 2012, 2014; Bertotti et al., 2017; Beaudoin et al., 2016, 2019, 2020a,b,c; Beaudoin and Lacombe, 2018; Labeur et al., 2021). In particular, the recent combination of SRIT applied to bedding-parallel stylolites with burial models allows estimation of the timing at which burial-related pressure-solution was active, granting valuable insights into the timing of subsequent tectonic phases (i.e. Beaudoin et al., 2020c; Lacombe et al., 2021) and past fluid migration (Beaudoin et al., 2020c; Labeur et al., 2021).

The scientific challenge of this study is to effectively combine latest techniques to accurately define and validate the chronology of porosity evolution in the early Cretaceous lacustrine carbonates of the TOCA Fm. in the Lower Congo basin, West African passive margin (Harris, 2000). The Lower Congo basin holds important oil and gas resources in offshore carbonate reservoirs, including the TOCA Fm. The syn-rift Barremian (130-125 Ma) carbonates of the TOCA Fm. exhibit extremely variable present-day porosities at a regional scale, with porosity values ranging from 1% to 30% depending on depositional textures, location within the basin and intensity of diagenesis (see details in Harris, 2000). In such a situation, it is of particular importance to understand and quantify the diagenetic processes, which have been most detrimental to reservoir quality, leading to porosities below 10% (i.e. generally admitted threshold for economic production). In this study, we investigated a well in which the TOCA Fm. exhibits present-day porosities of only 4–8% at 4069–4150 m burial depth in order to best demonstrate the added value of our new methodology and the relevance of our results to address the scientific challenge stated above. In this paper, we report an unprecedented multi-proxy approach which combine semi-quantitative estimates of the proportion and timing of porosity destruction related to (1) mechanical compaction by using a basin model (TemisFlow™), (2) diagenetic cement precipitation in pores, by means of thin-section image analysis, U–Pb ages and fluid inclusion microthermometry, and (3) pressure-solution based on quantification of chemical compaction along stylolites coupled with burial model. Each of these techniques embeds its own uncertainty but we consider that the combination of semi-quantitative methods reduces the global uncertainty on the resulting chronology of mechano-chemical events. This multi-proxy approach illustrates notably the added value of the information provided by SRIT in the understanding of porosity evolution in carbonate rocks and reservoirs.

2. Geological setting

2.1. Geodynamical history of the South Atlantic basins

The break-up of the supercontinent Pangea in Neocomian times (145-130 Ma) led to the separation of the African from the South American continents and the formation of the South Atlantic Ocean as a progressive northward opening of new oceanic domains (Mohriak et al., 2008; Matton and Jébrak, 2009; Pletsch et al., 2001; Szatmari and Milani, 2016). More specifically, concerning the evolution of rifting of the South Atlantic Ocean, several tectonic phases have been identified in the tectono-sedimentary architecture of the margins (Karner et al., 2003; Contrucci et al., 2004; Moulin et al., 2005). Nowadays, the South Atlantic can be divided into four segments from north to south (Torsvik et al., 2009; Moulin et al., 2010): the equatorial segment, the southern segment, the Falkland segment and the central segment, the latter being the focus of this study. The central segment is characterized by the presence of a thick salt layer approximately 1–2 km thick (Brognon and Verrier, 1966; Masson, 1972; Brice et al., 1982; Giresse, 1982; Teisserenc and Villemin, 1989; Aslanian et al., 2009), overlying a mainly continental sedimentary series (145-116 Ma). These series (pre-salt and salt) are overlain by marine clastics and carbonates (112 Ma to present-day) (Burk and Dewey, 1974; Doyle et al., 1982; Mussard, 1996). The history of the central segment can be divided into three main phases from the onset of rifting to the present day (below) (Da Costa et al., 1999; Aslanian et al., 2009; Beglinger et al., 2012; Chaboureau et al., 2013).

1) The syn-rift phase (Neocomian to mid-Aptian) marked by deposition of lacustrine and alluvial formations within graben and half-graben-like structural basins (Lehner and De Ruiter, 1977; Schoellkopf and Patterson, 2000; Beglinger et al., 2012). According to Brownfield and Charpentier (2006), the syn-rift basins are separated by basement highs and are internally organized as a series of asymmetrical horsts and grabens parallel to the present-day coastline.
2) The transition phase corresponds to a transitional cycle from active rifting to thermally-induced lithospheric subsidence affecting the South Atlantic basins (Gabon, Lower Congo and Kwanza basins; Fig. 1a) in the Aptian times, i.e., after crustal stretching, rifting and basement fault activity stopped (Uncini et al., 1998; Beglinger et al., 2012). This transient subsidence is marked by the “break-up unconformity” (BUU), when basin dynamics was controlled by thermal subsidence (Beglinger et al., 2012) and by 1–2 km thick evaporite deposition (Lehner and De Ruiter, 1977; Teisserenc and Villemin, 1989; Aslanian et al., 2009). Following Mohriak (2003), the BUU is linked to a period of peneplanation leading to a low residual topography. Early Aptian siliciclastic deposits from reworked uplifted and tilted Neocomian rift blocks mark this peneplanation episode. Late Aptian evaporites overly the clastic deposits (Burwood, 1999). Several studies have shown that the onset of salt deposition is probably linked to progressive marine transgressions in the proto-South Atlantic (Asmus and Ponte, 1973; Beglinger et al., 2012) and to more arid conditions (Bate, 1999; Karner and Gambôa, 2007).
3) The post-rift phase started at Albian times, and encompasses the separation of the two continents by continental break-up and subsequent oceanization (Aslanian et al., 2009; Guiraud et al., 2010; Beglinger et al., 2012). The post-rift phase is marked by a thermal subsidence (Guiraud and Maurin, 1991), a major regional marine transgression to the north and gravity driven salt tectonics (Lehner and De Ruiter, 1977; Dingle, 1999; Karner and Driscoll, 1999). Post-rift deposits are composed of ramp or shelf carbonates (deposited in shallow water), deep marine clastic, organic-rich black shales and local deltaic deposits (Séranne and Anka, 2005; Torsvik et al., 2009).

2.2. The Lower Congo basin: location and structural setting

The Lower Congo basin is located in the eastern margin of the central segment of the South Atlantic, between Gabon and Angola (Vernet et al., 1996; Harris, 2000; Aslanian et al., 2009). Two zones of low subsidence delimit the Lower Congo basin, referred to in the regional literature as “arches” and corresponding to oceanic fracture zones (Asmus and Ponte, 1973; Beglinger et al., 2012): the Mayumbe arch to the north and the Ambriz arch to the south. To the east, the basin rests unconformably on the Mayumbe Precambrian basement (Fig. 1a). The Congo margin part

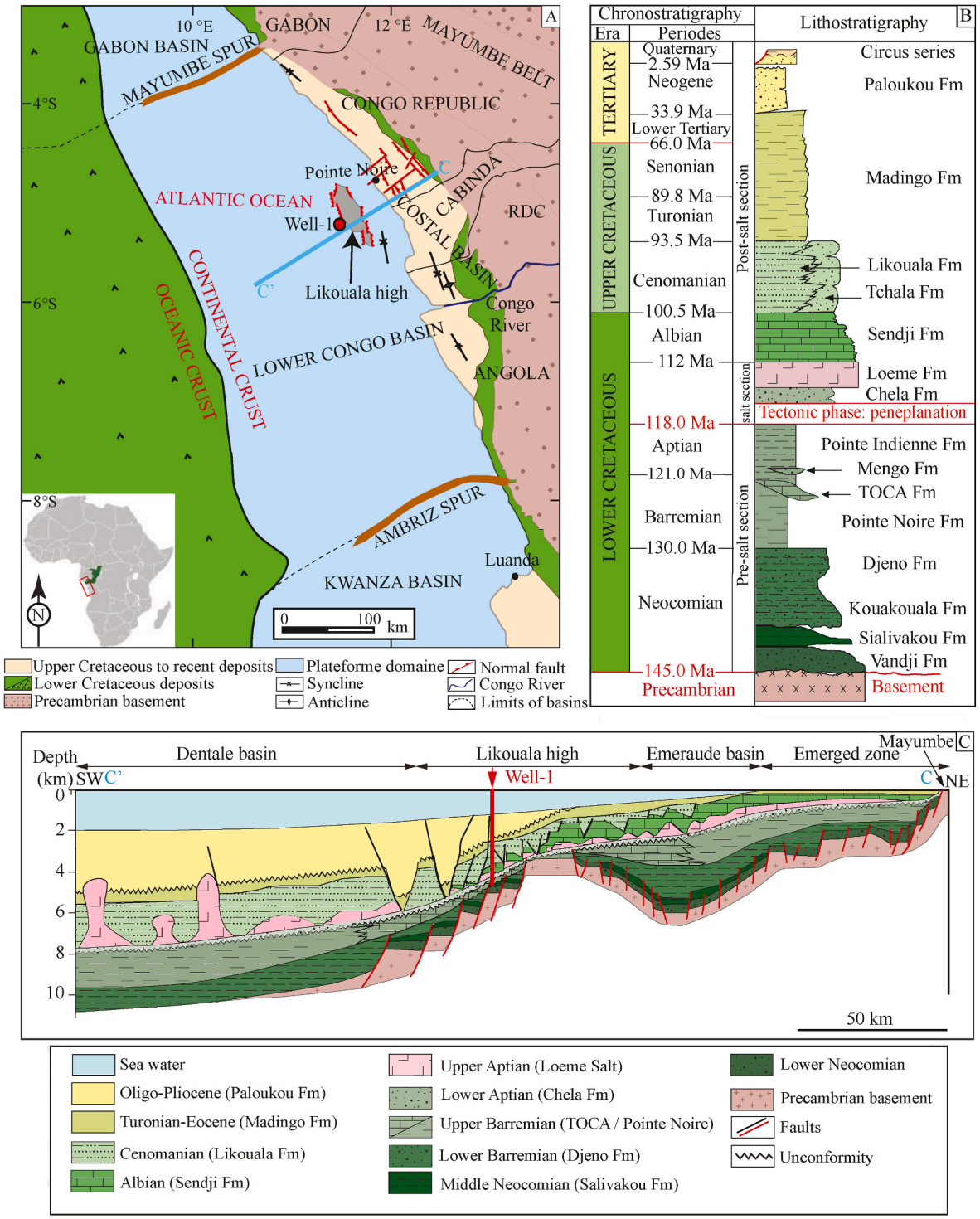

Fig. 1. (A) Structural map of Africa along the South Atlantic from Gabon to Angola with basins location. The green color in the marine domain represents the Cretaceous oceanic crust. (B) Stratigraphic chart of Lower Congo basin. (C) Regional geological cross-section through the Congolese margin. Modified after Vernet et al. (1996) (see 1a for section location). (For interpretation of the references to color in this figure legend, the reader is referred to the Web version of this article.)

of the Lower Congo basin extends from the SW of Gabon to the NE of Cabinda Province (Angola). The coastal basin, a vast (17 000 km^2, Desthieux, 1993) flat area of low elevation, is bounded to the east by the Mayumbe belt composed of terraced and levelled surfaces (Guillocheau et al., 2015) with an average elevation of 500 m and with peaks reaching 700–800 m. The Congolese margin is the offshore part of the coastal basin in the northern part of the Lower Congo basin. In the central Lower Congo basin (offshore Pointe Noire region; Fig. 1a), the syn-rift sediments are present in two zones: a proximal depocenter in the Emeraude basin and a distal depocenter in the Dentale basin, separated by the horst of Likouala (Fig. 1a & c) where the data analyzed in this paper were collected.

2.3. The Lower Congo basin: stratigraphy and sedimentology

The stratigraphy of the Lower Congo basin can be subdivided into

three main intervals from rifting to the present-day (Fig. 1b): (1) the pre-salt section (145-118 Ma), which consists of continental syn-rift sequence, (2) the salt section (118-112 Ma), which marks the major incursion of the South Atlantic Ocean into the rift (transition phase), and (3) the post-salt section (112 to present-day), which essentially consists of marine sequences deposited on the subsiding passive margin of West Africa (McHargue, 1990). Because Jurassic, Triassic and Palaeozoic series are missing (Bidiet et al., 1998), the Cretaceous-Cenozoic sedimentary series rests directly on the so-called Precambrian 'basement' (Fig. 1b & c), which comprises both the crystalline part of the Congo craton and the overlying Precambrian pre-rift sediments (Delpomdor et al., 2008; Mbina Mounguengui and Guiraud, 2009; Préat et al., 2010). Fluvial and lacustrine deposits dominate the syn-rift filling of the pre-salt basins (Guiraud et al., 2010), and were dated using ostracods, pollens and spores biozones (Grosdidier, 1967; Chaboureau et al., 2013). This study focuses on the Barremian lacustrine carbonates

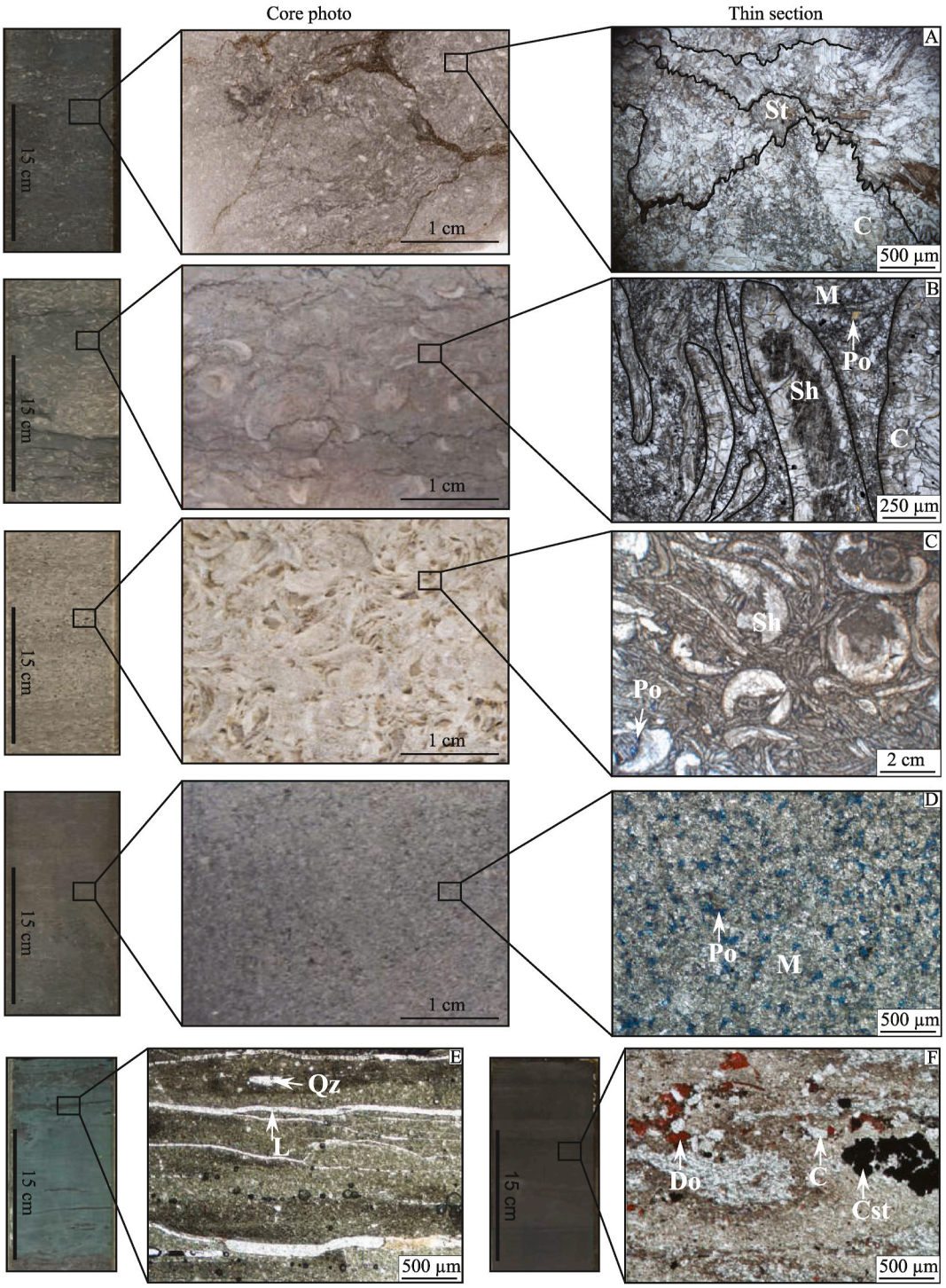

Fig. 2. Photographs of the Well-1 core showing different carbonate textures. (A) Wackestone to packstone texture; (B) matrix-supported coquina; (C) grain-supported coquina; (D) mudstone to wackestone texture; (E) green shales and (F) black shales. Po - pore; Sh – shells; C -Calcite cement; St – Stylolite; M – matrix; Do – dolomite; L – lamination; Cst – Clastic undefined fragment; Qz – Quartz fragment. (For interpretation of the references to color in this figure legend, the reader is referred to the Web version of this article.)

of the TOCA Fm. (TOCA for TOp CArbonates), a member of the pre-salt, syn-rift interval. The pre-salt interval starts with the Neocomian sandstones and clay of the Vandji, Sialivakou, Kouakouala and Djeno formations, which are overlain by the lower Barremian clay of the Pointe Noire Fm. (PN) (Fig. 1b) and the studied lacustrine carbonates of the TOCA Fm., deposited during the terminal phase of rifting. The late Barremian clay deposits of the Pointe Indienne Fm. overlie the PN and TOCA formations and are themselves unconformably overlain by the early Aptian sandstones of the Chela Fm. (Harris, 2000).

2.4. The studied area: The Likouala high

The Likouala high is located in the central part of the Lower Congo basin, at the border between Congo and Angola (Cabinda province) (Fig. 1a). The Likouala high (Fig. 1a & c) is one of the horsts formed in response to rifting. It has a submeridian orientation, is 50 km long and 20 km wide and is intersected by a series of troughs oriented between N40 and N180. The high separates two domains: the Emeraude basin to the northeast and the Dentale basin to the southwest (Fig. 1c). The Likouala high was a long-lived topographic high since the time of deposition of the Djeno Fm. until the end of the rifting period, with an intense erosion at the top of the high so that the Chela Fm. rests locally unconformably on the Berriasian Vandji Fm. (145–140 Ma, Chaboureau et al., 2013). The Likouala horst allowed the preservation of a low bathymetry environment and the development of the TOCA carbonates (Fig. 1c) (Unpublished data from TotalEnergies internal report).

E-W oriented seismic lines constrain the regional structure. Seismic data of the top of the horst reveal that the structure is a set of tilted blocks oriented NW-SE bounding a monocline. On this high, towards the NE, the carbonates of the TOCA Fm. wedge out under the Chela, either due to erosion or to a lack of deposition (Fig. 1c).

3. Materials and methods

3.1. Studied material

All observations were made and data were acquired from an 81 m long core within the TOCA Fm. sampled between 4069 and 4150 m depth in one offshore well (Well-1 in Fig. 1). Within this interval, we were granted access to a total length of 51 m (63%) of the cored section, distributed at various places along the entire core length. However, the core intervals we studied include all significant sedimentary textures representative of the entire core.

3.1.1. Core description

The carbonates of the TOCA Fm. exhibit several recrystallized sedimentary textures (Fig. 2). The TOCA Fm. was deposited in a shallow, lacustrine environment showing cyclical variation in water depth and a tendency to water stratification and oxygenation fluctuations (Unpublished data from Totalenergies internal report). It can be divided into three units based on biological features (Harris et al., 1994; Harris, 2000), from bottom to top: (i) TOCA 1 characterized by microbialites; (ii) TOCA 2 hosting microbial encrustations of shells, microbial mats and thrombolites; and (iii) TOCA 3 consisting in a substantial accumulation of granular and coquina texture, i.e. where constitutive elements consist mainly of freshwater lamellibranch tests belonging to the Unionidae group (Grosdidier et al., 1996). This study focuses on the TOCA 3 unit, which is characterized by the lowest porosity values encountered in the TOCA Fm. regionally (Harris, 2000). The identification of the AS9 Ostracod biozone (AS9 base ~130 Ma, AS9 top ~125 Ma) constrain the deposition age to the Barremian (Grosdidier et al., 1996; Bate, 1999; Gradstein et al., 2004). In addition to the diversity of textures, the TOCA Fm. shows numerous stylolites on the studied Well-1 core.

3.1.2. Stylolites

Stylolites are rough dissolution surfaces developing under the stress resulting from either burial compaction or tectonic shortening. In the former case, they are referred to as sedimentary stylolites and in the latter case to as tectonic stylolites. They are frequently observed in sedimentary rocks, namely carbonates (Stockdale, 1922, 1926, 1936, 1943; Dunnington, 1954; Bushinskiy, 1961; Park and Schot, 1968; Bathurst, 1972; Buxton and Sibley, 1981; Railsback, 1993). Stylolites are observed at different scales, from microscopic (grains, veins) to macroscopic (outcrop or core). A stylolite (Fig. 3) can be physically described by the amplitude, wavelength, and frequency of the peaks, parameters of which regularity permits to classify the stylolite based on its morphology, itself related to the growth rate of the stylolite (Koehn et al., 2016). The more recent morphological classification, which accounts for the effect of the stylolite on the local fluid flow, has been proposed by Koehn et al. (2016). For the sake of clarity, stylolite morphology distinguishes the shape of the base (greater-than mm) from infra-mm-scale peaks. Class 1 (rectangular) consists of a large rectangular base with low-amplitude peaks on the flat top of the rectangle. Class 2 (seismogram) is characterized by a narrow top-hat shaped base with low-amplitude peaks. Class 3 (suture and sharp peak) includes all stylolites with a flat or wavy base with locally high-amplitude peaks. Class 4 (wave) stylolites have a wavy base with scattered small peaks. Two other characteristics of stylolites have also been considered and further analyzed in this study: (1) the height of the biggest tooth with respect to an average baseline, which is a proxy for estimating compaction by dissolution along a 1D profile (Toussaint et al., 2018); and (2) the roughness (Renard et al., 2004), defined as the difference in height (dh) between two points, separated by a defined horizontal distance (dx) along the stylolite track (Fig. 3). The final stylolite roughness is acquired at the end of the stylolite development in a quasi-instantaneous process, independent of time and strain rate (Rolland et al., 2014).

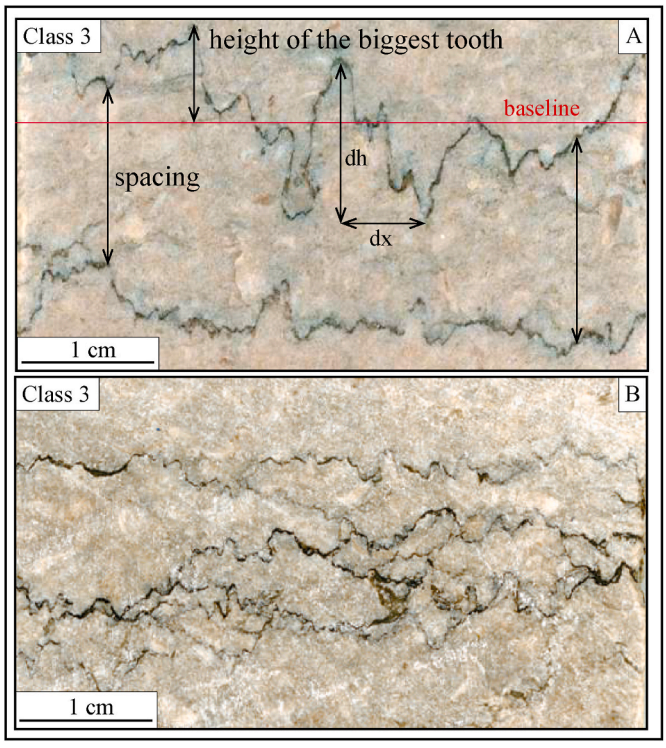

Fig. 3. Core photographs showing examples of class 3 stylolites: (A) – single, well-spaced stylolites and (B) – anastomosed stylolites. The stylolite roughness is defined as the difference in height (dh) between two points, separated by a defined horizontal distance (dx) along the stylolite track.

3.2. Methods

This section presents the different methods used to characterize the TOCA carbonates (petrography, fluid inclusion microthermometry, U–Pb dating) and to estimate the porosity destruction over time (mechanical compaction, cementation, chemical compaction).

3.2.1. Optical and cathodoluminescence microscopy

The petro-diagenetic study of the TOCA Fm. is based on the petrographic analysis of 57 thin-sections under a Zeiss Axioplot polarising microscope equipped with a Nikon Digital sight DS_U2/Ds_Fi1 camera. The diagenetic state of carbonates was further investigated under cathodoluminescence on a NewTec scientific Cathodyne model CATHOD-SP01 equipped with an IDS UI-3850CP-C-GL R camera (vacuum of 90 mTorr, 12–15 kV voltage and 200 μA intensity). All microscopic work was carried out at the laboratory facilities of the TotalEnergies technical and scientific center (CSTJF, Pau, France).

3.2.2. Elastic parameters of the TOCA textures from mechanical tests

In order to determine the mechanical properties of the studied carbonates, multitriaxial tests were conducted on two samples. A multitriaxial or multi-stage test is a triaxial revolution test during which the confinement is set to a given value, then the sample is brought close to failure, then the confinement is increased again. The cycle is repeated 3–4 times. This type of test allows several triaxial tests to be simulated with a single sample. The tests were carried out at TotalEnergies Geomechanical Laboratory (CSTJF, Pau, France). Two plug samples (38 mm diameter ×76 mm height) were carefully selected to ensure that the carbonate texture has not been deformed during burial history, and then were cut along the vertical axis of the core. The two selected samples include a wackestone and a packstone, i.e., the two carbonate textures most commonly encountered in the core.

Two multitriaxal tests were performed to evaluate the elastic properties of the rock: Young modulus and Poisson ratio. Three cycles were done per sample. Each plug was tested at 10, 30 and 50 MPa of confining stress. For each confining stress, an axial stress ramp was applied with a displacement rate of 0.01 mm/min until the yield point was reached, and then the deviatoric stress was unloaded with the same displacement rate at 0.01 mm/min to finalize the cycle. Axial and radial gauges measured deformations.

3.2.3. Stylolite distribution

The stylolite dataset comes from the 51 m studied from Well-1 core over a depth range between 4069 m and 4149 m (see section 3.1). In order to better understand the spatial distribution of stylolites along the entire core length, we conducted a statistical study of the stylolite density and their spacing. Only stylolites with a total visible length of at least 2 cm were considered in this study. Stylolite density was obtained by counting the number of visible stylolites along the core (for each sedimentary texture). Interpreted density values were obtained by normalizing the total number of stylolites in a given texture per meter length of this texture.

To measure the spacing, we drew two scanlines parallel to the core axis on the photos that intersect perpendicularly the tracks of the stylolites. Then we measured the spacing between the stylolites along these lines, stopping the measurement at each texture transition. The spacing was discontinuously measured along the core, in zones of stylolite clusters of maximum 30 cm thickness. The spacing between stylolite clusters exceeding 30 cm and the core sections devoid of stylolites were not considered. Statistical distribution of both stylolite density and spacing values were calculated considering the sedimentary texture.

3.2.4. Estimates of burial–related chemical compaction

The minimum amount of chemical compaction that stylolites accommodated was estimated from the height of the highest tooth along the 1-D profile (Koehn et al., 2016; Toussaint et al., 2018).

Digitized stylolite tracks were used with Matlab scripts modified after Ebner et al. (2009a). We first define the baseline position by calculating the average trend of the track, correcting it from the dip, and placing the extremities of the signal to 0. The height of all peaks (teeth) from the baseline is measured along the track, and the maximum absolute value is considered as representative of the minimal compaction accommodated along the plane, making the assumption that dissolution was evenly distributed. It is noteworthy that this approach is bound to be a rough underestimate of the true compaction, as (1) the maximum height on a tooth in a 1-D signal can miss bigger teeth on the 3-D plane, (2) this approach neglects the effect of the growth rate highlighted in Koehn et al. (2016); and (3) recent work shows that stylolite can dissolve without changing the morphology (Koehn et al., 2022). However, the latter study also states that the biggest tooth, if preserving the full dissolution, was a good estimate of the dissolution. On top of it, this approach, when applied on a large population of stylolites, yields results that are comparable at the first order to the loss of matter estimated by chemical mass balances (Toussaint et al., 2018).

Cumulating chemical compaction estimates along each stylolite plane of the entire population yields a rough minimal estimate of the total volume of dissolved rocks during burial. This is expressed as a percentage value of compaction with respect to a given texture as follows:

$$\%\ \text{compaction} = \frac{\sum (BPS)^{*}\text{Amean}}{\text{h}} * 100 \quad (1)$$

where h is the thickness of the sedimentary texture considered (m), A_{mean} is the mean value of the highest teeth for all stylolites identified in the carbonate texture (m) and $\sum$(BPS) is the number of stylolites in the carbonate texture.

3.2.5. Stylolite roughness inversion technique (SRIT) applied to sedimentary stylolites

The empirical study of single-track stylolites has shown that their roughness displays two regimes with self-affine properties, according to the scale of observation: one dominated by the surface energy at small-scale < 1 mm and the other by the elastic energy at large-scale > 1 mm (Renard et al., 2004; Schmittbuhl et al., 2004). By treating a stylolite track as a signal, signal analysis method such as Fourier transform returns two slopes, each defined by a specific roughness coefficient (Hurst coefficient). When the roughness is > 1 mm, the Hurst exponent equals 0.5, a value typical of elastic energy. When the roughness is < 1 mm, the related roughness coefficient is ~1.1, a value typical of surface energy (Ebner et al., 2009a, b, 2010b; Rolland et al., 2012, 2014).

From this observation, Schmittbuhl et al. (2004) derived a characteristic length at which the growth regime switches from being dominated by surface energy to being dominated by elastic energy. This cross-over length is defined as follows:

$$L_c = \frac{\gamma E}{\beta \sigma_m \sigma_d} \quad (2)$$

where Lc is the cross-over length (m); E the Young modulus (Pa); γ the solid-fluid interface energy (J.m^{-2}) and $\beta = \nu\,(1 - 2\nu)/\pi$, a dimensionless constant with ν being the Poisson ratio. For γ, we used the known value for calcite, $\gamma = 0.32$ J m^{-2} (Wright et al., 2001). The mean stress (σ_m, in Pa) and differential stress (σ_d, in Pa) are defined as:

$$\sigma_m = \frac{\sigma_1 + \sigma 2 + \sigma 3}{3} \quad (3)$$

$$\sigma_d = \sigma_1 - \sigma_3 \quad (4)$$

In the specific case of sedimentary stylolites, it is possible to consider the stress on the horizontal plane as isotropic ($\sigma 1 > \sigma 2 = \sigma 3$), leading to a simplified equation as:

$$\sigma_v^2 = \frac{\gamma E}{\alpha L_C} \quad (5)$$

with $\alpha = \frac{(1-2\nu)(1+\nu)^2}{30\pi(1-\nu)^2}$ (Ebner et al., 2009b).

The appropriate values of each parameter are needed to derive the vertical stress. The mechanical parameters (Young modulus and Poisson ratio) are derived from the mechanical tests.

Then it is possible to convert the value of σ_v (in Pa) into depth (m) using the following formula:

$$\sigma_v = \rho g h \quad (6)$$

with ρ the density of the host rock (2600 kg m^{-3}) and g the gravitational field acceleration (9.81 m s^{-2}), regardless of any assumption on the past geothermal gradient and fluid pressure (Toussaint et al., 2018; Beaudoin et al., 2019, 2020; Beaudoin and Lacombe, 2018).

In order to ensure that the in-plane stresses (i.e., the stresses in the plane of the stylolite) are equal, hence to test of the validity of the uniaxial strain hypothesis which allows the derivation of equation (5), three mutually oblique sections were cut perpendicular to the stylolites and were treated following the same inversion method (Schmittbuhl et al., 2004; Ebner et al., 2009b). If the resulting Lc values from the three cuts were found to be identical within uncertainty, the assumption was considered to be valid. On the contrary, the stylolites were not considered as sedimentary stylolites and were discarded from the dataset.

3.2.6. Burial-time model

We have built a burial-time model to reconstruct the burial evolution of the TOCA Fm. over time using TemisFlow™ basin modelling software. The present-day geometry to be simulated is based on the formation top-base depths, as measured in Well-1 data. We defined the properties of each lithology (porosity, permeability) from the Well-1 and the geological events (erosion) described from the seismic interpretation (TotalEnergies internal maps). Two erosional events are described in the field: (1) early Aptian (~75 m) related to the peneplanation of the Likouala high and (2) early Tertiary (~100 m) related to the global uplift of the margin. The ages of these two erosional events were estimated on the basis of unpublished seismic interpretations from TotalEnergies. The chronostratigraphic column (Table 1) shows the list of the 14 layers considered for this study, each of those being characterized by the age at which deposition begun and ended, by a thickness and by a lithology. Restored geometries can be edited further by entering an estimate of erosion (in m) and paleo topography or paleo-bathymetry maps. The physical properties of each layer (initial porosity, solid density; Table 1), as well as the constitutive laws (compaction) are defined with respect to the ratio of the different sedimentary textures (limestone, shale, sandstone) described in the layer.

The backstripping process allows for the inversion of the evolution of the basin geometry through time using a 1-D backward modelling (Perrier and Quiblier, 1974). The simulation begins in the present day and ends when only the substratum remains. In this case, the simulation is finished at −145.5 Ma, which corresponds to the age of the basement top.

For each period defined in the chronostratigraphic column (Table 1), we removed what has been deposited and added what has been eroded as defined from the seismic data. After sedimentation and erosion have been accounted for, the remaining sedimentary formations are decompacted, or compacted (in the case of erosion), by using porosity vs depth curves calibrated empirically for each lithology. The porosity vs depth curve for the carbonates used in the TemisFlow™ software is taken from literature data for conventional endmembers: Schmoker and Halley (1982) for micritic carbonate of the mudstone to wackestone type; Bebout (1974) for grainstone type carbonates with no fine fraction and with early diagenesis and Scholle (1977) for chalk.

For modelling the evolution of the porosity, the key controlling factors are the compaction parameters. The calibrated porosity vs depth empirical law used in the simulation represents porosity evolution controlled by both mechanical compaction (grain framework tightening) and early chemical compaction (bioclast dissolution along grain-to-grain contacts due to pressure-solution). For the sake of simplicity, we will describe hereinafter the mechanical tightening and the early chemical micro-seams developing at grain contacts altogether as mechanical compaction, and the mesoscale stylolitization as chemical compaction. The backstripping is performed considering the hydrostatic pressure regime and the porosity vs depth law.

The forward modelling provides access to the evolution of the geometry of the 1-D column, and to the associated porosity in each layer.

3.2.7. Fluid inclusion petrography and microthermometry

Fluid inclusions are sealed cavities filled with water, oil, gas and/or solid phases occurring in minerals. They can form during/soon after crystal growth (primary inclusions or pseudo-secondary inclusions) or later as a result of crystal microfracturing and healing (secondary inclusions) in the presence of a fluid. They constitute a microsample of the paleo-fluid present in the pore space at the time of their formation (Roedder, 1984). The aim of our fluid inclusion work was to identify the different populations of fluid inclusions present in the samples, to analyze their distribution and abundance, and to determine their melting and homogenization temperatures ($T_{m\ (ice)}$ and T_h) in order to constrain the nature of the mineralizing fluid.

Four samples were prepared as double polished 150 μm thick sections glued on a petrographic glass slide using acetone-dissolvable superglue. For microthermometric analysis, the rock wafer must be removed from the glass slide in order to fit on a 6 mm quartz disc within

Table 1
Chronostratigraphic column used for the study presented here. The simulation begins at −145.5 Ma and ends at the present day. The basin model input parameters such as age; present-day thickness and initial porosity of each formation are indicated.

Event		Age (Ma)		Thickness (m)	Initial porosity (%)	Solid density (kg/m3)
Lithology/Event	Number	From	To			
Paloukou	14	33,9	0,0	1833,9	59,6	2,65
Erosion	13	65,5	33,9			
Lower Tertiary	12	65,5	33,9			
Madingo	11	93,5	65,5	207,0	59,6	2,65
Likouala	10	99,6	93,5	605,8	48,1	2,70
Upper Sendji	9	103,0	99,6	417,2	56,4	2,68
Lower Sendji	8	112,0	103,0	527,9	54,2	2,66
Loeme	7	116,0	112,0	60,0	9,4	2,20
Chela	6	118,0	116,0	45,0	62,3	2,65
Erosion	5	118,0	117,0			
Pointe Indienne	4	123,0	118,0	90,0	62,3	2,10
TOCA/Pointe Noire	3	130,0	123,0	129,0	51,5	2,69
Djeno	2	141,0	130,0	117,0	51,5	2,65
Basal sandstones	1	145,5	141,0	90,0	51,5	2,65

the heating/cooling stage. The rock wafers were separated from the glass slides by dissolving in acetone for one night. Each wafer was then carefully cleaned.

The fluid inclusion microthermometry study was performed by H-Expertise Services (HES), Nancy, France. The petrographic study, based on optical observations by polarized light and epi-UV fluorescence, was performed with the goal to describe the different fluid inclusion populations within a petrographic context (host cement, limit grain-overgrowth, overgrowth, and fracture cement), their petrographic origin (primary fluid inclusion, intragranular or transgranular fluid inclusion planes), the content and abundance of each phase (water, gas or oil) and the relative timing relationships (contemporaneous versus not contemporaneous aqueous and oil inclusions). Only fluid inclusion populations showing the petrographic characteristics of primary fluid inclusions (following Goldstein and Reynolds, 1994) were selected for microthermometric measurements.

The epi-UV fluorescence observations were conducted using a Zeiss AxioImager.A1m microscope with an excitation filter centered at 365 ± 5 nm and an emission filter long pass around 400 nm. Phase transitions observed in two-phase fluid inclusions were recorded over a LINKAM MDS 600 heating-freezing stage (min. −170 °C, max. 400 °C) equipped with a Sony Exwave HAD3 color video camera mounted on an Olympus BX 51 microscope at GeoRessources, Vandœuvre-lès-Nancy. The microthermometric stage was thermally calibrated using CO2 synthetic fluid inclusions standards for melting temperature $T_{m\ (CO2)}$, H2O synthetic fluid inclusions standards for $T_{m\ (ice)}$ and cross-calibrated natural alpine fluid inclusions ("home" standard) for T_h. The accuracy of measurements is estimated at ± 0.2 °C for $T_{m\ (ice)}$ (heating at 0.5–1 °C/min) and ±0.5 °C for T_h (heating at 1–5 °C/min). To avoid stretching problems related to freezing, the measurements of the homogenization temperatures were done prior to the measurements of ice melting temperature on the same sample.

3.2.8. U − Pb dating of the calcite cement

The U–Pb dating of the interstitial calcite cements was carried out at Center Européen de Recherche et d'Enseignement des Géosciences de l'Environnement (CEREGE), Aix-en-Provence, France using a LA-ICP-MS-HR. The equipment consists of an ArF 193 nm, 4 ns excimer laser: (ESI, Elemental Scientific Industries) and an HR-ICP-MS with magnetic sector (Element XR, Thermo fisher). Measurements were performed following a methodology analogous to Godeau et al. (2018).

Analyses were conducted on five thick (~100 μm) polished sections exhibiting large areas of the sparitic cement of interest. The samples were placed in the sample cell and scanned (3200 dpi resolution) for easy navigation from one piece to another on the instrument software.

A screening phase was first conducted to investigate U and Pb concentrations and U/Pb ratio variation over the entire thick section in order to select the best areas for the final measurements (Roberts et al., 2020). Analyses were done with a laser spot size of 150 μm. The ablation speed is of the order of 1–1.5 μm/s under standard conditions, it is preceded by a pre-ablation phase of a few seconds to clean the sample surface. Samples were measured by a standard bracketing approach, using the NIST-614 glass standard for instrumental drift and lead isotope composition (Woodhead and Hergt, 2001) and the WC-1 natural calcite standard for inter-elemental fractionation (reference age = 254.4 ± 6.4 Ma; Roberts et al., 2017). A total of 24–48 ablation spots were performed for each microsite analyzed. Detailed spot-by-spot assessment was carried out afterwards by examining ablation pits under CL microscopy.

The U–Pb isochrone ages were calculated in a Tera-Wasserburg diagram using the Isotplot 4.15 add-on (Excel).

3.2.9. Phase estimates by image analysis

Eight thin-sections were cut perpendicularly to the bedding in the core. In order to quantify the amount of the various diagenetic cements observed in the samples, we conducted a 2-D image analysis based on interpretations from optical (PPL) and cathodoluminescence (CL) microscopy observations. Thin-section wide photomosaics of the most representative texture, i.e., packstone, were assembled for eight samples located at different depths along the core. The pictures were performed under the same exposure conditions for all thin-sections to ensure the representativeness and comparability of data. We used the Fiji software for performing a manual picking based on combination of the luminescence of each pixel on the CL image and on the color of the minerals on the corresponding PPL image. Emphasis was put on quantifying the most important calcite cements (C1 and C2, see below) which fill the interbioclast and intrabioclast (bivalve shell filling) porosity. The very minor occurrence of aragonite shell cement was not quantified.

4. Results

4.1. Macroscopic and microscopic observations and sedimentary texture description

4.1.1. Petrogenetic description

Following observations on core and thin-section, five different sedimentary facies were identified, referred to as F1a, F1b, F1c, F2a and F2b described below, and grouped into two main types: bioclastic facies (F1) and mudstone facies (F2). They are characterized by their mineralogical and paleontological content and their sedimentological characteristics (texture, grain size, etc.). The latter mainly comprises Lamellibranchs of the Unionidae family (freshwater characteristics), and Ostracods (Grosdidier et al., 1996; Bate, 1999; Gradstein et al., 2004). It is notable that in all the observed facies, the amount of clayish mineral is negligible.

Facies F1a (Fig. 2a) consists in bioclastic limestone composed of broken shells of Ostracods and Pelecypods (rare ooids) in a micritic matrix, occurring as grainstones to rudstones. Shells are generally composed of macrosparitic calcite while the matrix is microsparitic. F1a is highly stylolitized and tight.

Facies F1b (Fig. 2b) consists in bioclastic limestone composed of poorly sorted Unio shells and Gastropods in a microsparitic matrix, occurring as wackestones to floatstones. This facies is highly stylolitized and mainly tight. One plug porosity measurement (total Phi) has been performed on this texture and shows a porosity of <2%.

Facies F1c (Fig. 2c) consists in bioclastic limestone composed of brocken or preserved Unio shells, Gastropods and rare Oncoids in a microsparitic matrix, occurring as packstones to rudstones according to the abundance of the shells. Most of the shells are recrystallized either into a macrosparite or into a microsparite. This facies exhibits intergranular and intercrystalline macroporosity visible in thin-sections. Plug measurements yielded total porosity ranging from 4 to 8% and averaging 6% (n = 14) porosity.

Facies F1b and F1c are overwhelmingly predominant representing about 90% of the cored section. They are mainly composed of packstones. Facies F1c (packstones) accounts for 70% of the studied section in Well-1 core.

Facies 2a (Fig. 2d) consists in microsparitic calcareous mudstone (mudstones to wackestones), with rare scattered debris of Gastropods and Ostracods. The matrix is a homogeneous microsparite. This facies occurs in very low amount along the Well-1 core.

Facies 2b (Fig. 2e and f) consists in microsparitic calcareous mudstone, with scattered crystals of pyrite crystals, and rare quartz grains (silt) and dolomite rhombs, occurring as green shales or black shales.

4.1.2. Diagenetic description

Thin-section examination by optical (LPNA) and cathodoluminescence (CL) microscopy allowed identification of several diagenetic events (Fig. 4 & Fig. 5). These diagenetic events include, in chronological order, shell micritization, aragonite to calcite neomorphism, precipitation of blocky calcite C1, mechanical compaction, precipitation of blocky calcite C2, and chemical compaction. In

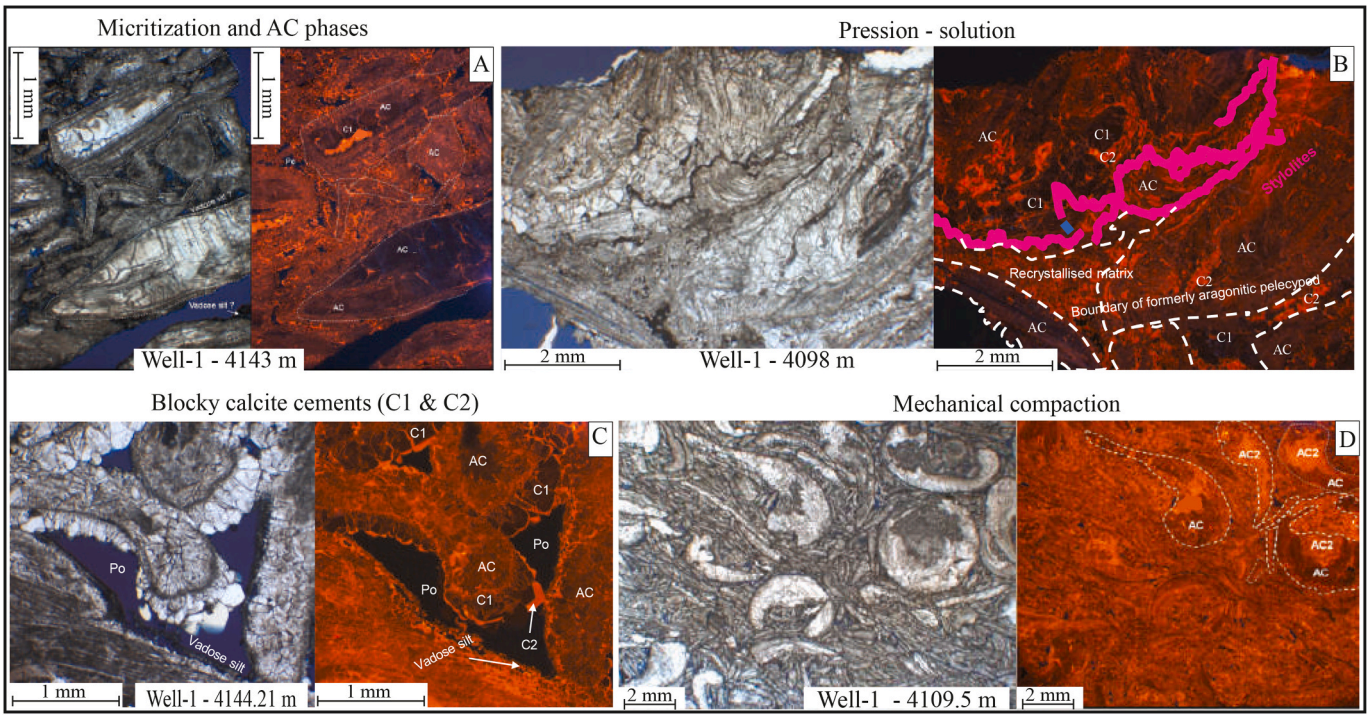

Fig. 4. Examples of diagenetic events of the TOCA Fm. (A) Eogenetic phase (AC) and vadose silt in F1a facies; (B) pressure-solution (stylolite) in F1b facies; (C) early and late cementation in F1b facies; (D) mechanical compaction expressed by broken shells in F1c facies. AC – aragonite to calcite; C1 & C2 - blocky calcite cement and Po – pore.

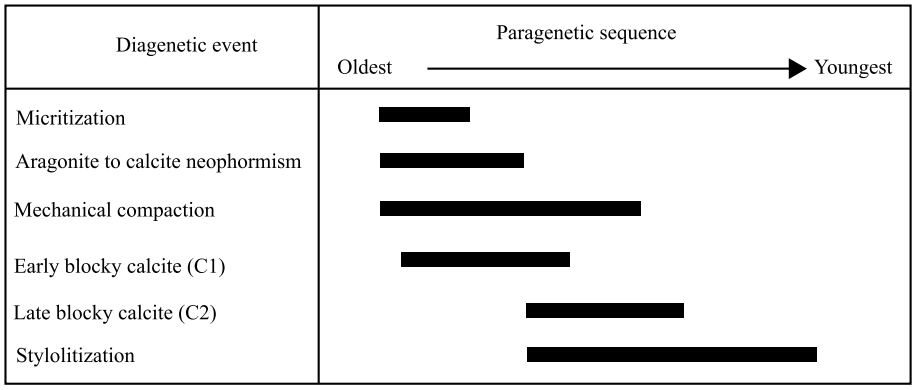

Fig. 5. Diagenetic sequence of the TOCA Fm. at Well-1- core.

accordance with data reported by Harris (2000), our samples of the TOCA 3 interval show very little visible secondary porosity limited to rare residual dissolution voids within aragonite bioclasts (that were not entirely filled by blocky calcite cement C1) and very minor leaching of C1 calcite crystals locally. The remaining secondary dissolution was not precisely quantified but is estimated to represent on the order 0.5% at most (see Fig. 11c for illustration). Consequently, the main diagenetic transformations observed in thin sections appear to have either no effect (micritization, neomorphism) or a negative effect (compaction, cementation) on reservoir properties.

The micritization is common in the grainstone facies and is the earliest stage of the paragenetic sequence. Micrite mostly developed around bivalve shells and ooids. The diagenetic phase AC (Fig. 4) corresponds to the neomorphism of the aragonite of gastropod and pelecypod shells into calcite. It shows a black to dark brown cloudy luminescence under cathodoluminescence. The blocky calcite cement C1 (Fig. 4a, b & 4d) develops inside and around the bioclasts, i.e., as intrabioclast and interstitial cement. Under cathodoluminescence, C1 is non-luminescent (dull to dark brownish color). The mechanical compaction is expressed by the breaking (Fig. 4c) and microfracturing of bioclasts and is not homogeneous in intensity along the core; it is more developed and visible in grain-supported facies. The mechanical compaction affects the early cement (AC and C1). The calcite C2 cement postdates calcite C1 and is characterized by a rather bright orange cathodoluminescence (Fig. 4a, b & 4d). Mesoscale stylolites developed in these intervals affect all the calcite cements (Fig. 4b), indicating that stylolitization prevailed/continued after C1 and C2 precipitation.

The compaction-related pressure-solution appears to have been active throughout a large part of the diagenetic history (Fig. 5). It developed first along discrete pressure-solution seams and micro-stylolites along contacts between bioclasts as a result of stress increase during mechanical compaction. As previously mentioned, the process encompassing both the mechanical and the early grain-contact-limited chemical compaction (micro-stylolites and seams), which prevailed before and slightly after early C1 cementation, will be referred to as 'mechanical compaction' hereinafter. In contrast, the compaction-

related pressure-solution occurring along widespread mesoscale stylolites and affecting both the bioclastic material and the cements C1 and C2 will be referred to as 'chemical compaction'.

In summary, three main significant mechanisms operated during the diagenetic history (Fig. 5) to control the evolution of the reservoir porosity, all in a negative way: (1) mechanical compaction, expectedly mostly efficient during early burial; (2) (early) precipitation of intra-bioclast and interstitial cement (e.g., C1 and C2) and (3) chemical compaction through the mesoscale stylolitization and the likely precipitation of the dissolved material in the vicinity of the stylolites (eventually filling the remaining porosity). Although, these mechanisms developed in sequence they likely overlapped significantly and may have affected each other to some extent. For instance, the early calcite cementation (C1) may have delayed/limited the subsequent mechanical compaction by increasing framework rigidity.

4.2. Sedimentary stylolite distribution

In the investigated 51 m depth interval, a total of 615 stylolites was counted in the different carbonate textures. The distribution of stylolites in relation to sedimentary texture (Fig. 6a) shows that stylolite density (number of stylolites per m length) is greater in wackestones (median = 20) than in mudstones (median = 13) and packstones (median = 8). The complete statistical data are shown in Table 2.

4.3. Chemical compaction along stylolites

As already reported, a minimum estimate of the dissolution due to chemical compaction along a stylolite track is provided by the height of the highest tooth with respect to the baseline (Fig. 3a; Beaudoin et al., 2016; Koehn et al., 2016). It is noteworthy that the distribution of tooth heights (Fig. 6b) shows a first-order correlation with sedimentary textures. The lowest heights are found in mudstones, with a median value of 2.5 mm, while the wackestones and packstones show similar distributions, with median values of ~4.4 mm.

Table 2
Statistics of the density of stylolites along the Well-1 core.

Statistics of the density of stylolites (number/m)			
	Mudstone	Wackestone	Packstone
minimum	0	0	0
median	13	20	8
maximum	80	175	90
mean	22	31	9
mode	20	0	0
standard deviation	21	48	16

The cumulated linear thickness of the different carbonate textures along the 51 m core investigated is 4 m, 8 m and 28 m for mudstone, wackestone and packstone, respectively, for a total length of 40 m. The other textures covering the remaining 11 m were not investigated due to the very low number of stylolites (grainstones) or the absence of stylolites (black/green shales). The percentages of chemical compaction (equation (1)) in the different carbonate textures are as follows: 5.4% for mudstones (over 4 m), 4.1% for packstones (over 28 m) and 13.6% in wackestones (over 8 m) (Fig. 6c). Considering the 40 m interval investigated by SRIT, the total percentage of chemical compaction is around 6.1% (i.e. ~2.5 m linear). Because of the limited number of maximum tooth heights measured (analysis performed on 44 stylolites considered representative of the 615 stylolites identified in the studied core section), we estimate that the uncertainty on the overall percentage of chemical compaction is ±30% (relative). Consequently, the minimum estimate for the total chemical compaction is considered to be between 4.3 and 7.9%.

4.4. Rock mechanics test

The results of the geomechanical tests (Table 3) show that the Young modulus E increases with confining pressure. E values are systematically

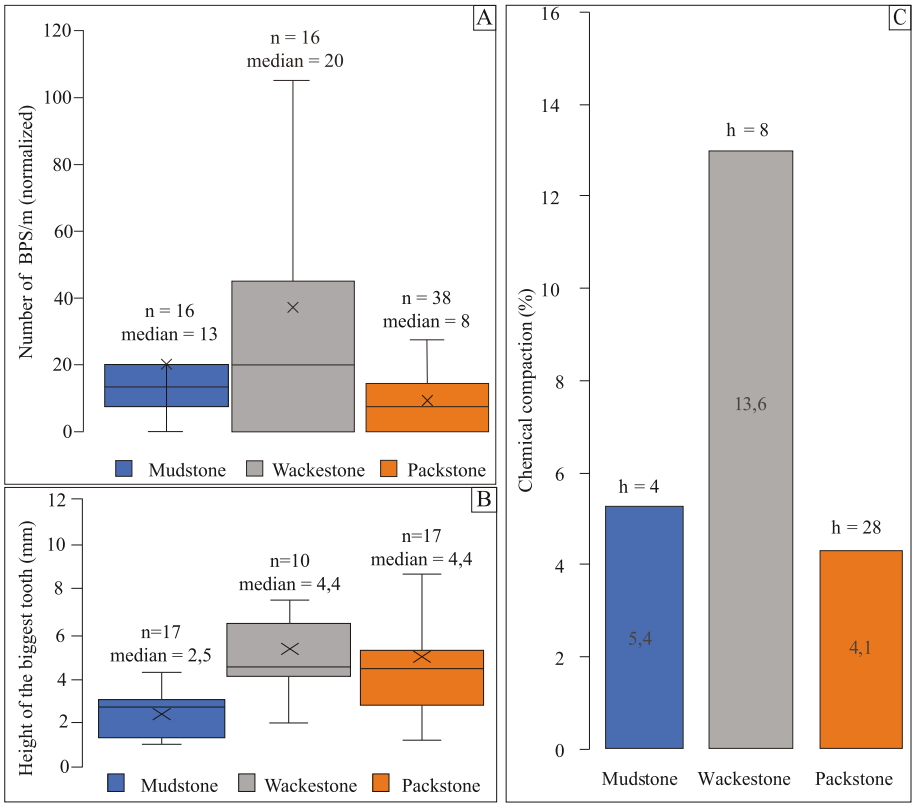

Fig. 6. Box-and-whiskers plots of the normalized number of Bedding-Parallel Stylolites (BPS) per meter (A) and the distribution of the height of the biggest tooth along a BPS track (B) as a function of the sedimentary texture. Distribution is reported from bottom to top: first decile, first quartile, median value, third quartile and ninth decile. (C) Percentage of chemical compaction calculated from eq. (1). The mean height of the biggest tooth are 2.3 mm; 4.9 mm and 4.9 mm for mudstone, wackestone and packstone textures, respectively. n- number of occurrences; h - thickness of each carbonate texture observed and measured on the core (in m).

Table 3
Elastic properties of the wackestone and packstone of the TOCA Fm. determined from rock mechanics tests.

Sample depth (m)	Core sedimentary facies	Young Modulus (GPa)			Poisson ratio		
		Cycle 1	Cycle 2	Cycle 3	Cycle 1	Cycle 2	Cycle 3
4086,66	Pelecypod Wackestone	21,4	27,9	33,3	0,30	0,22	0,19
4135,00	Pelecypod Packstone	28,1	31,4	35,2	0,30	0,25	0,21

higher in packstone than in wackestone textures. The Poisson ratio ν does not show any significant variation except for cycle 1, for which the determination of the ratio was difficult due to poor data quality.

The mean values of the elastic parameters determined from the tests are E = 30 GPa and $\nu = 0.23$. The uncertainty on the determination of E and ν is ±10% and ±20%, respectively.

4.5. Results of stylolite roughness inversion

Thirty samples were studied, in which 44 sedimentary stylolites (mainly class 3 and few class 4) were analyzed using the Fourier Power Spectrum (FPS) method. Only 27 stylolites (class 3) displayed two self-affine regimes with the expected Hurst coefficients, corresponding to a success rate of 61% (Table 4).

Fig. 7a shows four examples of processing. Three (Fig. 7 a1, a2 & a3) are acceptable because the inversion provides a trend showing two well-marked slopes with Hurst coefficients consistent with those predicted by the growth model. In contrast, Fig. 7 a4 shows a case of non-acceptable data because the inversion provides a monotonic trend with no change in slope.

For the stylolite roughness inversion, we used the mean values of the elastic parameters determined from the geomechanical tests (Table 3): E = 30 GPa and $\nu = 0.23$. The cross-over length (Lc) is given within ±23% uncertainty (Rolland et al., 2014).

After calculating the value of the vertical principal stress at the time pressure-solution along the considered stylolite stopped (equation (5)), the corresponding maximum depth was calculated (equation (6)). The 14–43 MPa range of σ1 values obtained for the 27 stylolites converts into a depth range of 550–1750 m. This information is presented as a violin plot in Fig. 7b, which is similar to a conventional box plot but takes into account the data distribution and the probability density (Hintze and Nelson, 1998 and references therein). Fig. 7b shows that the dissolution along 90% of the stylolites halted between 800 and 1600 m.

We also investigated if the carbonate texture may have an impact on the SRIT reliability for class 3. The results show that the highest Lc values are associated with the packstone texture, with a median value of 1.2 mm, while the mudstones and wackestones show much lower median values of 0.46 mm and 0.54 mm, respectively (Fig. 7c). This result reflects a significant effect of the sedimentary texture on the reconstructed Lc. Packstones appear to better record stylolites formed at medium depths, while mudstones and wackestones record a wider range of Lc values reflecting stylolites formed over the first burial phase.

4.6. Burial-time model

The burial-time model shows three phases of burial evolution over time (Fig. 8): (1) 130 Ma to 95 Ma, a first phase of rapid burial (~63 m/Ma) associated with the early Cretaceous rifting episode and an erosion phase. This major erosional event observed at 118-117 Ma, represents a margin uplift with a peneplanation event (as seen in Fig. 1b). The estimated subsidence of 63 m/Ma is an average value between the moderate burial rates of the first 500 m and the abrupt increase in the following ~2000 m. (2) 95 Ma to 35 Ma, a plateau with a low burial rate (~5 m/Ma) ending with an erosional phase in the Lower Tertiary; (3) 35 Ma to present-day, a second phase of rapid burial (~42 m/Ma) before reaching the present-day depth. Fig. 8 also shows the histogram plot of the maximum depths of active pressure-solution along bedding-parallel stylolites obtained from the roughness inversion.

Table 4
Results of stylolite roughness inversion for stress, applied to bedding-parallel stylolites in the TOCA Fm. The Lc value was calculated with an uncertainty of 23%. σv is calculated with values of E = 30 GPa and $\nu = 0.23$ determined from rock mechanics tests.

Samples	Textures	Class	Cross-over length (mm)	σv (MPa)	Depth (m)
4069,09-1.2 A	Mudstone	3	0,46	38	1550
4069,92-2 B	Mudstone	3	0,46	38	1550
4069,92-3 A	Mudstone	3	1,72	19	750
4074,30-1.1 A	Mudstone	3	0,69	31	1250
4074,30-1.1 B	Mudstone	3	0,58	33	1350
4074,30-1.2 A	Mudstone	3	0,37	42	1700
4074,30-1.2 B	Mudstone	3	0,38	41	1650
4074,30-2.2 B	Mudstone	3	0,44	38	1550
4074,30-3.2 B	Mudstone	3	0,64	32	1300
4074.30–4.2 B	Mudstone	3	0,63	32	1300
4074,30-2.1 A	Mudstone	3	0,78	29	1200
4074,30-2.3 A	Mudstone	3	0,43	39	1600
4079,40-1 A	Packestone	3	1,19	23	950
4079,40-1 B	Packestone	3	0,99	26	1050
4079,40-2.1 A	Packestone	3	1,29	22	900
4079,90-2 A	Packestone	3	1,05	25	1000
4079,40-2 B	Packestone	3	0,53	35	1450
4079,90-2 B	Packestone	3	1,20	23	950
4087,52-B1	Packestone	3	1,57	20	800
4097,54-2 A	Wackestone	3	0,54	35	1450
4112,27-1 B	Packestone	2	1,27	23	950
4113-1.1 A	Packestone	3	3,10	14	550
4131,14-A1	Wackestone	3	1,05	25	1000
4131,14-A2	Wackestone	3	0,47	37	1500
4137,09-1.1 B	Wackestone	3	1,13	24	1000
4137,09-1.2 B	Wackestone	3	0,36	43	1750
4148,59-A	Packestone	2	0,66	31	1250

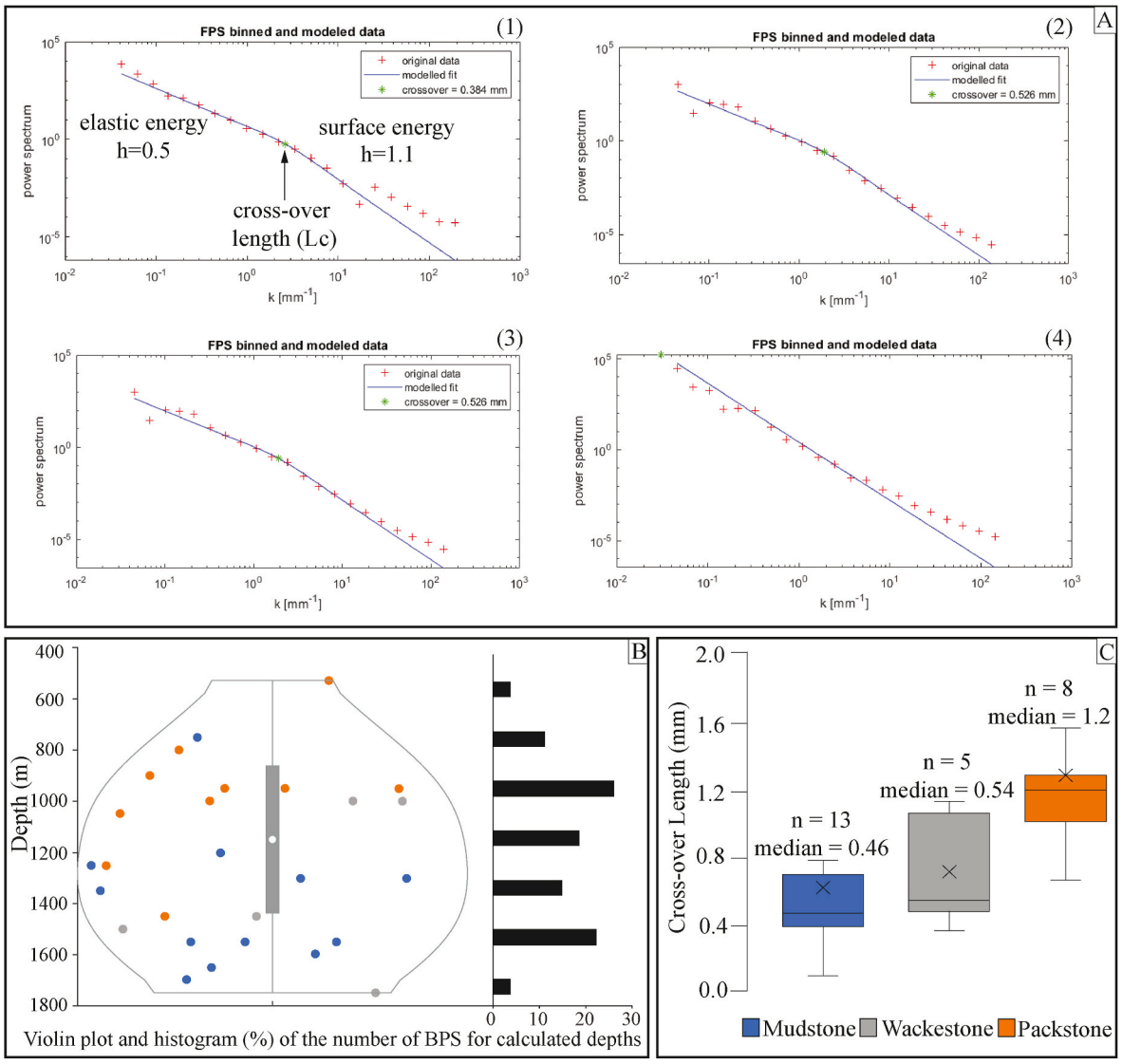

Fig. 7. (A) Definition of the Hurst exponent and cross-over length on a log-log plot of the Fourier Power Spectrum method (1) and examples of sedimentary stylolite roughness inversion for some samples, either successful (2 and 3) or failed (4). (B) Violin plots of the maximum depth of active pressure-solution derived from magnitude of vertical stress from stylolite roughness inversion and associated histogram (in %) of the data used for the violin plot. The blue, grey and orange circles represent class 3 stylolites in mudstone, wackestone and packstone textures respectively. (C) Box-and-whiskers plots reporting the value of the cross-over length obtained from the stylolite roughness inversion technique applied to the bedding-parallel stylolites versus carbonate texture for class 3 stylolites. n-number of occurrences. (For interpretation of the references to color in this figure legend, the reader is referred to the Web version of this article.)

4.7. Fluid inclusion microthermometry

Fluid inclusion microthermometry measurements could only be done on small to medium-size aqueous two-phase fluid inclusions (±5–25 μm) in calcite C1 cement. No oil inclusion was observed in the samples. T_h temperatures range from 80 to 160 °C and salinities from 300 to 360 g/l ($T_{m\ (ice)}$ range between −25.9 and −21.7 °C). All the measured T_h values are lower or close to the bottom-hole present-day temperature for the TOCA Fm. (~157–164 °C). The T_h data (Fig. 9a) illustrate a well-marked mode around ~120 °C, which may represent the main period of carbonate cementation. The measured salinities are well grouped at very high values of 300–360 g/l. The plot of salinity versus T_h (Fig. 9b) shows a large variation in T_h values with little or no variation in salinity, suggesting trapping of the same pore water over a wide temperature range. This data distribution brings up the question of a possible resetting of T_h values during subsequent burial, in particular in light of the U–Pb ages which indicate that the calcite C1 cement formed sub-syn-depositional (section 4.8). We note however the following observations: (1) the T_h histogram is well defined and rather symmetrical around a mode at 110–130 °C; (2) the mode is rather large ("flat") and 30–40 °C lower than present-day temperature; (3) the overall range of T_h values is very large, i.e., 67–158 °C; (4) only the very highest T_h value (158 °C) approaches present-day temperature (164 °C); (5) there is no evidence of heterogeneous trapping phenomena, i.e. boiling or two-phase fluid, in particular no report of vapor-rich inclusions eventually homogenizing to vapor; (6) there is no spatial control on the distribution of T_h values within calcite crystals. Consequently, the FI data are compatible with precipitation of the C1 calcite from a highly saline brine at variable temperatures, with a major phase around 110–130 °C. Alternatively, it cannot be totally excluded at this time that C1 formed at lower temperature (possibly as low as 70–80 °C) and that fluid inclusion were largely but not completely reset during subsequent burial by stretching (120 °C corresponding to the temperature prevailing during the long late Cretaceous-early Tertiary burial plateau).

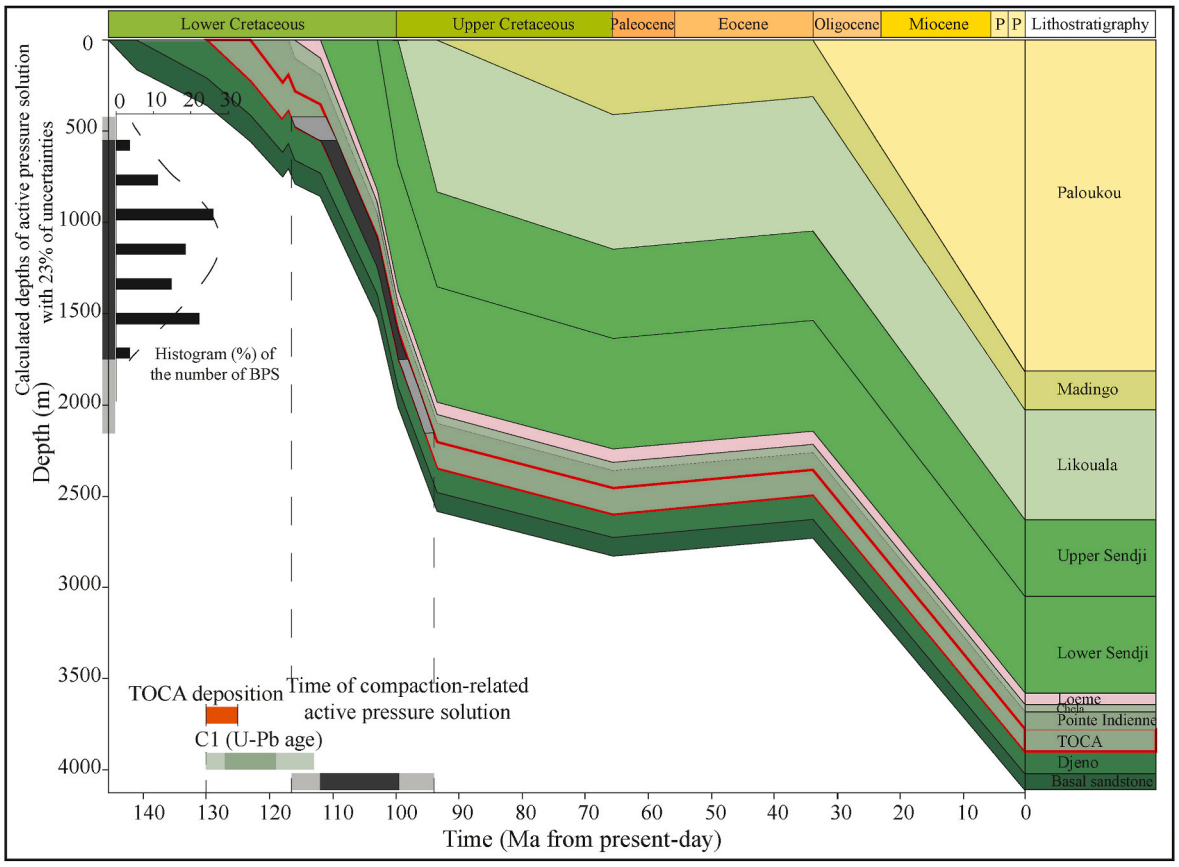

Fig. 8. Burial model constructed from Well-1 data corrected for mechanical compaction. The depth on the model is counted from the sea-bed. The calculated depth range of active pressure-solution from bedding-parallel stylolite inversion is reported for the TOCA Fm. as grey levels on the y-axis. The corresponding timing (with uncertainties in light grey) is reported on the x-axis.

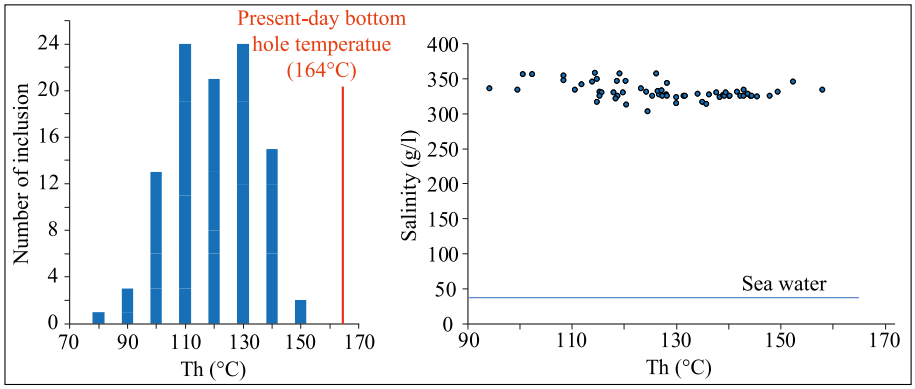

Fig. 9. Histograms of homogenization temperatures and salinity data from fluid inclusions.

4.8. U–Pb dating of the calcite cement

Only the early calcite C1 cement provided reliable U–Pb ages (Fig. 10). The late C2 cement could not be dated because of a low U–Pb signal. Two ages measured on the intrabioclast C1 cement yielded 127.4 ± 2.2 Ma and 123.13 ± 7.7 Ma (Fig. 10 a, b). Three ages measured on the intergranular C1 cement gave 125.7 ± 5.0 Ma, 123.35 ± 10.4 Ma and 119.4 ± 6.4 Ma (Fig. 10 c, d, e). All these ages are indistinguishable from each other within error, yielding an average age of 125 Ma basically identical to the upper age limit for the TOCA Fm. deposition.

The Tera-Wasserburg diagrams for the C1 cement displayed in Fig. 10 show an excellent alignment of individual data points, providing a very precise isochron age. Some minor data scatter is observed in the less radiogenic samples (Fig. 10c, d, and 10e). The isochron in Fig. 10c being the most affected by scatter (highest MSWD), it may be considered as providing a somewhat less accurate age than other samples, although indistinguishable within analytical error.

The U–Pb ages indicate that the C1 cement precipitated syn-depositionally or extremely early in the TOCA diagenetic history (considering TOCA Fm. deposition between 130 and 125 Ma). The complete dataset is available in the supplementary material.

4.9. Cement distribution estimates

Image analysis reveals that C1 calcite represents 25–30% (average 28%) of the thin-section surface depending on the sample, and C2 calcite

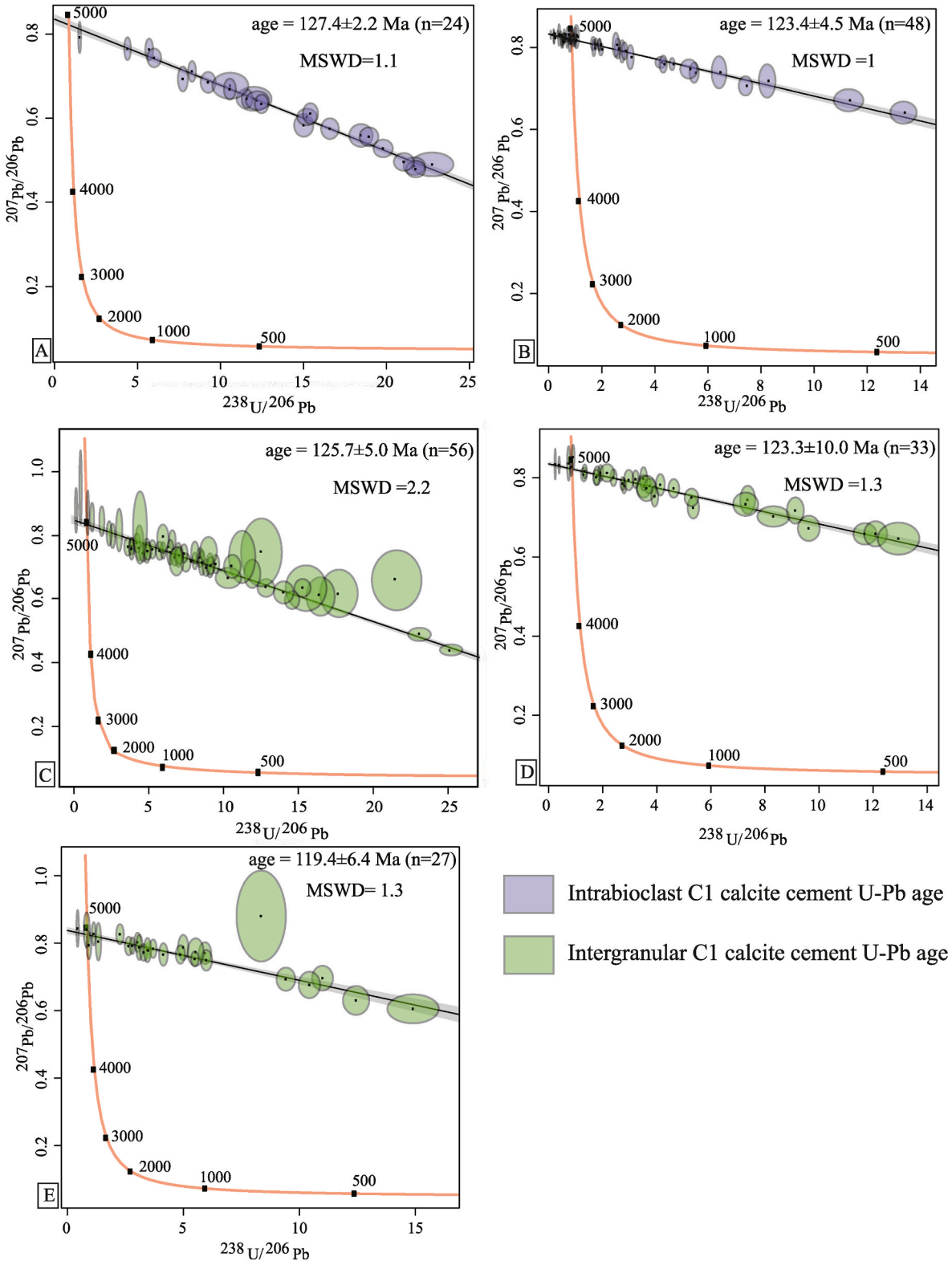

Fig. 10. Examples of the Tera-Wasserburg Concordia plots with the dated calcitic phase from TOCA carbonate formation. Intrabioclast C1 calcite cement U–Pb age (A and B) and intergranular C1 calcite cement U–Pb age (C, D and E). n – number of spots; MSWD - mean square of weighted deviates.

15–20% (average 17%) (Table 5). Fig. 11 shows that the intergranular C1 cement (~29%) is significantly more abundant than the intergranular C2 cement (~15%).

In order to assess repeatability and to reduce uncertainty in the results, we performed 3 different color calibration of the Fiji software for each of the eight thin-sections. However, because of the potential errors associated with picking C1 and C2 cements, and considering that the selected thin-sections may not be fully representative of the entire core, we estimate the uncertainty on the image-analyzed surfaces to be ±25%. This leads to an overall range of 19–38% (average 21–35%) for

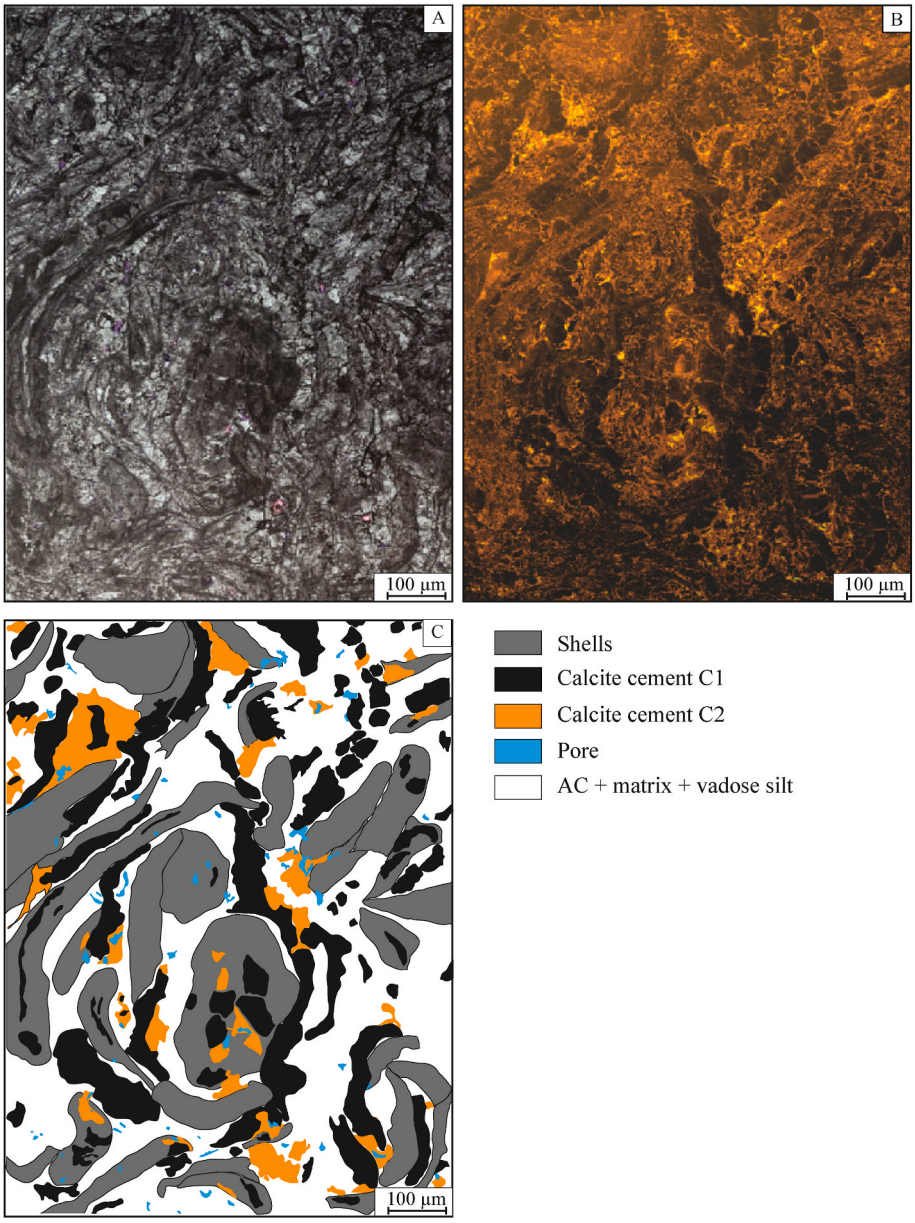

Fig. 11. Example of thin-section showing the different diagenetic phases. LPNA (A) and CL (B) image of the thin-section. (C) Line drawing underlining early calcite C1 (black), late calcite C2 (orange), shells (grey); residual porosity (blue) and other diagenetic processes/features (AC, matrix, micrite, microporosity; in white). (For interpretation of the references to color in this figure legend, the reader is referred to the Web version of this article.)

Table 5
Estimates of abundance of diagenetic cementation phase. The values represent the percentage of surface area of each phase in the considered thin-section.

Depth (m)	C1 (%)	C2 (%)
4126,92	26	20
4130,09	30	17
4132,05	29	15
4132,87	25	20
4139,87	29	15
4141,90	30	15
4145,90	25	20
4148,08	30	15

the C1 calcite and 11–25% (average 13–21%) for the C2 calcite.

Note that the porosity derived from image analysis of packstones (see Fig. 11c) reflects the visible macro-porosity only. It differs from the present-day total porosity (4–8%) determined on plugs for the packstone texture, because the micro-porosity associated to the microsparitic matrix cannot be quantified from Fiji image analysis.

5. Interpretation of results

5.1. Paragenetic sequence of the TOCA Fm. on the Well-1 core

The TOCA Fm. carbonates have been interpreted as lacustrine deposits presenting two distinct depositional environments: (1) a shoreline dominated by waves and rich in coquinas and (2) a palustrine system with episodic storm deposits. From the core and thin-sections, we established the paragenetic sequence that affected the TOCA Fm. since its deposition. The main diagenetic events that affected the TOCA Fm.

and had an impact on the reservoir quality are summarized below. Five major diagenetic processes are identified (Fig. 5):

1 Diagenesis started with a phase of partial to total calcification of the aragonite of the shells of bivalves in an eogenetic environment. This aragonite to calcite neomorphism AC resulted in the formation of shell replacive sparitic calcite crystals (Fig. 4a). The replacement of aragonite occurred rapidly and very early. In cathodoluminescence, neomorphic AC calcite is readily recognized by its brown to dark orange luminescence with a cloudy aspect. The aragonitic parts not replaced by AC have been dissolved later and are now either empty (as rare residual dissolution voids) or more generally cemented by the lately formed diagenetic calcites as described below. The occasional diagenetic micrite observed around the bivalve shells is more specifically common in grainstones and is the earliest stage of the paragenetic sequence. This micritization is attributed to microorganisms living near the sediment-water interface. These two phenomena (AC neomorphism and biogenic micritization) had no significant impact on the evolution of porosity.
2 The diagenetic cementation phase started with the precipitation of the first blocky calcite cement (C1) in the pores, resulting in a significant reduction of the interstitial porosity (both intergranular and intrabioclast). C1 precipitated in the voids (intergranular pores) and around AC (Fig. 4c), but textural relationships suggest that AC and C1 calcites may have developed partly synchronously. Cement C1 is affected by microfractures due to mechanical compaction (described below) and shows some minor dissolution affecting crystal outlines locally. C1 blocky calcite precipitated shortly after (or during) the dissolution phase of the biogenic aragonite not replaced by AC. The very high salinity (300–360 g/l) of the fluid inclusions in C1 indicates precipitation from hyper-saline water. This contrasts with the presence of freshwater fossils (Lamellibranchs (Unionidae group), Ostracods) in the TOCA Fm. which indicates that the lake water was not very salty. The U–Pb age (~125 Ma) indicates that C1 cementation occurred syn-depositionally or extremely early after deposition (130-125 Ma). The precipitation of C1 cement has an important impact on porosity reduction estimated to be in the range of ~25–30% (based on image analysis data). The relative volumes of C1 cement filling intrabioclast secondary porosity after shell dissolution (see event 1) and C1 cement filling original primary intergranular porosity are not known.
3 The mechanical compaction is expressed by microfracturing and breaking of bioclast shells that develop from the grain boundaries and propagate into the AC and C1 (Fig. 4d). The mechanical compaction is responsible for most of the poronecrosis observed in the intervals not affected by early calcite cementation. Mechanical compaction in the core parts where C1 is present appears to be very minor, suggesting that the framework rigidification resulting from extensive C1 cementation may have significantly inhibited mechanical compaction in these intervals.
4 The late blocky calcite cement (C2) precipitated after mechanical compaction during burial. The calcite crystals are orange under cathodoluminescence (Fig. 4c). The C2 cement is observed all along the studied depth interval with variable ratios. C2 often developed as overgrowths over C1 in the intergranular porosity and after all biogenic aragonite has been dissolved (or replaced by AC). The small amount of microfractures occurring in C2 suggests that burial was still moderate when C2 formed, which is consistent with precipitation either shortly after C1 in a slightly different diagenetic context or a somewhat later at the very beginning of burial diagenesis. The blocky calcite C2 represents ~15–20% of porosity loss in volume (based on image analysis).
5 The chemical compaction (117-95 Ma) is expressed by pressure-solution (mesoscale stylolites) which is best developed within those intervals that were not affected by the early cementation event (C1). The chemical compaction mainly postdates C1 and C2 cements, and represents a volume loss estimated to be on the order of 6%.

Petrographic and cathodoluminescence observations provide no evidence of any late corrosion-dissolution of the early calcite cements that could have produced secondary porosity and rejuvenated some reservoir quality.

Noteworthy, all the diagenetic processes described above took place prior to about 95 Ma (or 2500 m depth), in other words, during the first phase of burial preceding the late Cretaceous to early Tertiary subsidence idling (see above and Fig. 8).

5.2. Porosity evolution during burial

In this section, we estimate the contribution of each diagenetic event to the destruction of the porosity in the Barremian TOCA Fm. during burial, by quantifying the porosity reduction associated to mechanical compaction, early diagenetic cementation (C1 and C2) and pressure-solution reprecipitation (117-95 Ma). Moving back in time from the present-day porosity value, we then further propose a rough estimate of the initial porosity of the TOCA Fm., taking as an example the packstone texture.

Starting from a present-day average porosity value of 6% (average value obtained from geomechanical tests on 14 plugs of packstones ranging from 4% to 8% porosity) and assuming that 100% of the carbonate dissolved following chemical compaction by stylolitization (6 ± 2%) has reprecipitated in the intergranular porosity, we estimate that the porosity was 12 ± 2% before chemical compaction (Fig. 12). The reduction of the porosity by pressure-solution is of about 50%, which is in line with conservative estimates of Koehn et al. (2016). As cements C1 and C2 together represent 45 ± 11% of the rock volume, this implies that the porosity before calcite cement precipitation was 57 ± 13%, i.e. between 44 and 70% (Fig. 12).

The calculation above needs to be considered as a first order semi-quantitative estimate. It takes into consideration global uncertainties associated to some of the parameters (i.e., range of porosity values, amount of dissolution along stylolites, image analysis quantification of C1 and C2). However, other uncertainties exist that cannot be evaluated from current data. First, the calculation does not take into account that part of the C1 calcite has filled secondary pores after shell dissolution. Second, the use of the bigger teeth of stylolites to estimate chemical compaction leads to a minimum estimate of the carbonate volume dissolved along stylolites. Third, 100% of the material dissolved along stylolites has probably not precipitated on site. The underestimate of dissolution related to chemical compaction may to some extent be counterbalanced by the overestimate of reprecipitation of the dissolved carbonate material, but this cannot be ascertained. Our study does not permit to provide a more accurate quantification of the cumulative error on the reconstructed path of porosity evolution at this time, but this does not impair the importance of our results and the value of our methodology as discussed below.

To estimate the contribution of mechanical compaction to early porosity reduction, we used the total porosity-depth curve for packstone to grainstone as accounted for in the basin model TemisFlow™ and used for the burial-time model (Fig. 8). Considering an oldest depositional age of 130 Ma and that the major early cementation event (C1) occurred at 125 Ma, we can estimate the contribution of the early mechanical compaction to porosity reduction during the first ~5 Ma before C1 precipitated and prevented further significant mechanical compaction. This corresponds to a porosity reduction of ~2% (much of which might have affected preferentially the matrix microporosity), so the initial porosity was at about 59 ± 13% (i.e., between 46 and 72%; Fig. 12).

In spite of the methodological uncertainties associated with the estimates of mechanical and chemical compaction as well as with the amounts of C1 and C2 cements, this initial porosity estimate appears to be reasonable for a packstone carbonate depositional texture (Choquette

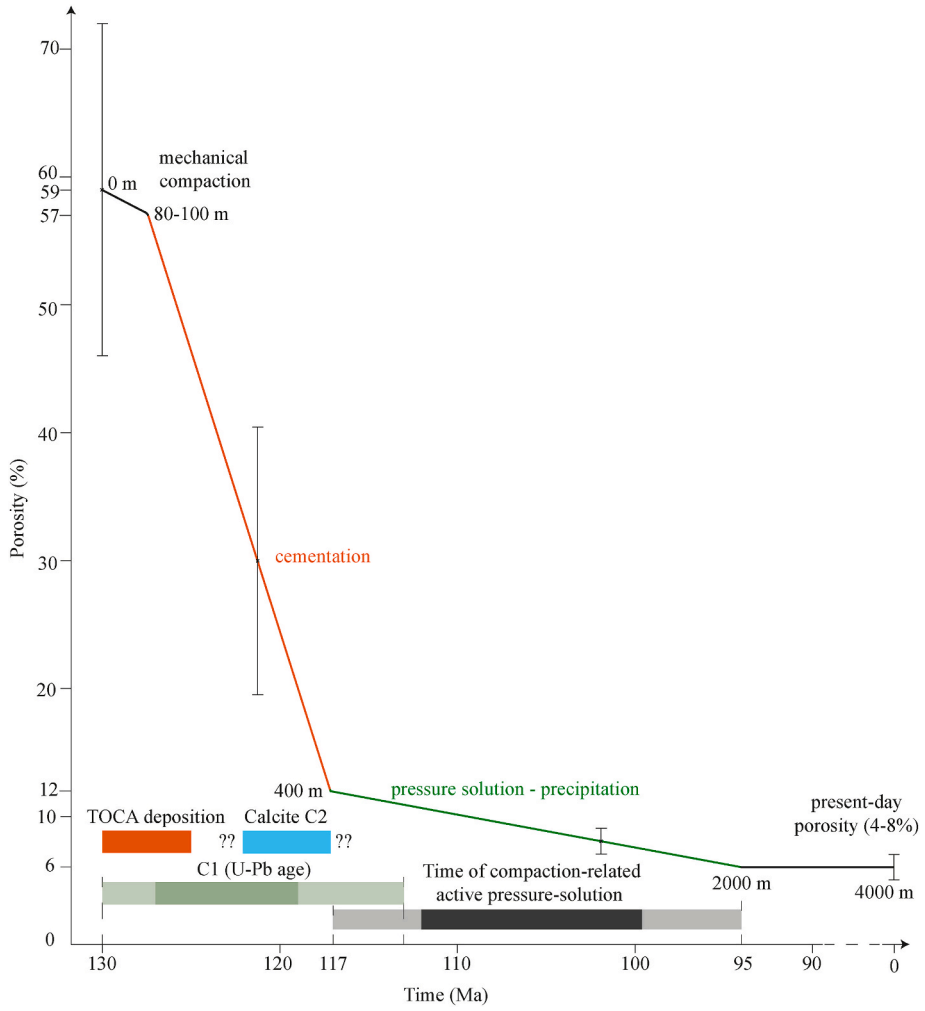

Fig. 12. Porosity evolution over time of TOCA Fm. Vertical lines in each part of the curve indicate the range of possible porosity values according to the estimated uncertainties.

and Pray, 1970; Schmocker et Halley 1982) and overall, falls within the range of initial porosities of 40–70% for carbonate sediments reported in the literature (Choquette and Pray, 1970). They are also consistent with the initial porosity values reconstructed by the TemisFlow™ software (Table 1).

Beyond this estimate of the porosity reduction, the important information from the above calculations is that the porosity has been drastically reduced over the first 10 Ma, primarily by cementation rather than by mechanical/chemical compaction. Porosity loss due to C1–C2 cementation alone represents about 75% of the depositional porosity (Fig. 12). The pressure-solution process then additionally reduced the residual porosity by ~50% to reach its current value at the end of the chemical compaction at about 95 Ma and 2500 m burial depth. This implies that the reservoir quality did not significantly evolve during the last ~100 Ma despite continuing burial to nearly 4000 m depth.

6. Discussion

6.1. Impact of carbonate textures on stylolite distribution and paleopiezometry

The distribution of the stylolite population in the studied core reveals that in term of density, mudstones are more prone to develop a dense network of stylolites compared to packstones and wackestones. Yet, the greater density of stylolites is documented in mud-supported, grain-rich wackestone, an observation in line with the ones of Xu et al. (2022). The relationship between stylolite initiation and texture is supported by the role of muddy-carbonate interface on the initiation of dissolution (Aharonov and Katsman, 2009). That role complements the known facilitating role of the clayish minerals on the initiation of dissolution under pressure (Carozzi and Bergen, 1987; Renard et al., 1997). While the stylolite initiation and density are seemingly affected by the texture, the amount of chemical compaction on a single stylolite is relatively stable with respect to textures (2.5 mm–4.4 mm, Fig. 6b). When considering the whole population, we estimated a minimum compaction of ~6%, which is consistent with the results of Vandeginste and John (2013) (7–12%), Koehn et al. (2016) (3–5.6%) and Ehrenberg et al. (2016) (5–9%). This consistency suggests that the amount of chemical compaction accommodated by pressure solution is about 10% in carbonate rocks, regardless of the context. At a closer look, in the case of the TOCA Fm., the wackstone texture is more efficient in accommodating vertical shortening by pressure solution.

The results from stylolite roughness inversion highlight an effect of the sedimentary texture on the reconstructed Lc values (Fig. 7c). Indeed, it is striking that the class 3 stylolites Lc values are significantly different between mud-supported textures (mudstones and wackestones) for which the Lc value is lower (median = 0.5 mm), and grain-supported textures (packstones) for which the Lc value is significantly higher (median = 1.2 mm). We can tentatively link this result to the role of grain size in the stylolite development. Koehn et al. (2016) demonstrated that the amount of dissolution was inversely proportional to the grain size of the material undergoing dissolution. In other words, the

smaller the grains, the greater the chemical compaction, because smaller grains offer a larger reaction surface in the rock. Consequently, in mud-supported carbonates where the average grain size is smaller than in grain-supported carbonates, the dissolution might last longer, and SRIT may return greater depths of active pressure solution.

This new dataset suggests that a reliable estimate of the maximum burial depth at which compaction-related pressure solution was still active using class 3 stylolites would require the analysis of these stylolites within mudstone. We believe this novel indication will help establish the application of this developing method.

6.2. Origin of fluids associated with early cementation of the TOCA Fm

Fluid inclusions indicate that C1 calcite cement precipitated from hot (or moderately hot if resetting occurred) highly saline fluid. The age of the C1 cement (~125 Ma) indicates a very early precipitation in the burial history, certainly before the formation reached 200–300 m burial. Considering a sea-bed temperature of 13 °C based on paleo bathymetric map (Unpublished data from TotalEnergies internal report) and a paleo geothermal gradient documented for the early Cretaceous times of 27–30 °C/km (Robert and Yapaudjian, 1990; Baudino et al., 2018; Macgregor, 2020) would result in a burial temperature of ~25 °C at 400–500 m depth, i.e., much lower that the range of 80–160 °C suggested by fluid inclusion thermometry (Fig. 9). Consequently, we infer that the parent waters of the C1 cement were most likely of hydrothermal origin. The T_h values should therefore not be interpreted as reflecting the burial depth of the TOCA Fm. at the time of C1 formation. A possible origin of the hydrothermal and hypersaline fluids could be the Neoproterozoic evaporite formations (Schisto-Calcaire Subgroup) which have been documented in the underlying pre-rift basement by field studies conducted in the continental part of the Lower Congo basin (Delpomdor et al., 2008; Préat et al., 2010). Such occurrence of Neoproterozoic evaporites has also been proposed by Kadima et al. (2011) based on well and geophysical data. In such a scenario the hypersaline hydrothermal fluids would have migrated upward along major basement-rooted syn-rift normal faults, invaded the porous carbonates at shallow depth and probably partially reached the lake water locally.

6.3. Evolution of porosity in the TOCA tight carbonate reservoir and implication for hydrocarbon exploration

In the coquina facies studied in Well-1 core, the macroscopic porosity is diverse in nature, being interparticular, intercrystalline, moldic and vuggy. This porosity is largely cemented by the C1 calcite cement. Together with the eogenetic AC phase, this early cementation has limited mechanical compaction and pressure-solution, and possibly later fluid-rock interactions during burial. In contrast, in other core sections where early diagenetic events (AC and C1) were less important, numerous stylolites are observed and the interparticle porosity was mainly destroyed by mechanical compaction. In the studied core section, porosity was further reduced by later precipitation of blocky calcite C2 as well as by the likely precipitation of the material dissolved along bedding-parallel stylolites. Although not observed in the studied section bitumen occurring as pore-fillings has been reported in other sections of the Well-1 core, and would constitute an additional cause of poronecrosis in the TOCA limestone (Unpublished data from TotalEnergies internal report).

Our results show that early cementation governed the evolution of porosity in the TOCA (Fig. 12). This is consistent with the results of Xu et al. (2022) on bioclastic limestones from the Middle East which support that early cementation is the controlling factor for compaction and subsequent dissolution under pressure in the reduction of porosity. Our results show that the present-day porosity of the TOCA carbonates (~4–8%) in the studied well was acquired very early during the diagenetic and burial histories and has probably not evolved much since the end of pressure-solution at 95 Ma, i.e., since the formation has reached 2500 m depth (Fig. 12). This is supported by the absence of evidence of any significant corrosion-dissolution of the early calcite cements in the core that could have produced secondary porosity and rejuvenated some reservoir quality (the minor secondary porosity formed by very early dissolution of parts of the aragonite shells was rapidly filled by C1 cementation). This suggests that fluid-rock interactions in the reservoir were strongly limited due to the low (connected) porosity remaining after the massive early cementation. Early diagenetic cementation therefore appears to be the main controlling factor of the evolution of reservoir porosity in the packstone carbonates of the TOCA Fm. This conclusion is in line with the observations made by Harris (2000) in the coquina facies of the upper part of the TOCA Fm. from offshore cores provided by Elf Congo and Chevron. The sedimentological observations of Harris (2000) showed that the upper TOCA unit (TOCA 3: coquina facies, which is the TOCA unit investigated in this study in the Well-1 core) shows poor reservoir qualities. Harris (2000) reports that the best TOCA reservoirs regionally are primarily found in TOCA 1 (microbialites) and TOCA 2 (microbial encrustations of shells, microbial mats and thrombolites) facies units. Our results provide an explanation for the generally poor quality of TOCA 3 reservoirs in the studied area of the Lower Congo basin (Well-1 is located within the regional perimeter considered by Harris, 2000). Our observations from Well-1 indicate that the initial porosity in the TOCA 3 unit (coquina facies) was largely destroyed during early burial, well before hydrocarbon migration in the TOCA Fm. (see more discussion below), resulting in making the TOCA 3 unit a regionally poor reservoir. Note that this steady and fast decrease in porosity during burial (Fig. 12) suggests that the creation of porosity by dissolution is far less important than porosity occlusion during burial diagenesis. The major role played by early cementation in the reduction of porosity in the TOCA carbonates support the results of other studies (Ehrenberg and Nadeau, 2005; Xu et al., 2022).

It is well known that the relative timing of the hydrocarbon migration into the reservoir and of the mechanisms that preserve/create or destroy porosity is key for the appraisal of the petroleum system. When early cementation remains limited, mechanical compaction may reduce the porosity progressively during burial, allowing some residual porosity to be available at the time of potential hydrocarbon charge. In contrast, despite its delaying/inhibiting effect on mechanical compaction, massive early diagenetic cementation may reduce most (>78% relative) of the porosity even during shallow burial (first 500 m), thereby strongly limiting the amount of porosity available later at the time of hydrocarbon migration into the reservoir. The hydrocarbon migration in the TOCA reservoirs in the Lower Congo basin is mainly dated from the Cenomanian to the Paleocene (i.e. after 95 Ma) (Schoellkopf and Patterson, 2000; Brownfield and Charpentier, 2006; Beglinger et al., 2012). The hydrocarbon migration into the TOCA reservoir therefore occurred after the initial porosity had been largely destroyed, resulting in the tight nature of the TOCA reservoir in Well-1. This hydrocarbon migration is also concomitant with the end of the development of the population of bedding-parallel stylolites, hence the role of the increase of the local (i.e. at the dissolution interface scale) fluid pressure by the hydrocarbons can be questioned in the halting of the development of the stylolites.

7. Conclusions

This study unravels the history of porosity destruction over time in the tight, deeply buried early Cretaceous (130-125 Ma) lacustrine carbonates of the syn-rift TOCA Fm. in the Lower Congo basin (West Africa passive margin). The main conclusion are summarized below:

- An original multi-proxy approach was adopted to unravel the burial and diagenetic history of the TOCA Fm. This approach includes simulation of a burial model, U–Pb dating and fluid inclusion thermometry of diagenetic cements and inversion of the roughness of the

sedimentary stylolites for maximum burial depth of active chemical compaction.

- The absolute age of the key paragenetic events controlling reservoir properties of the TOCA Fm. have been constrained: mechanical compaction (~130-127 Ma based on TemisFlow™), early cementation (~125 ± 5 Ma based on U–Pb dating on calcite diagenetic cement), and chemical compaction (~117-95 Ma based on stylolite roughness inversion). This provides new constraints on the diagenetic sequence of the TOCA Fm. and a better understanding of the diagenetic processes and their absolute timing, which is a key information for a better prediction of the reservoir properties in exploration.
- All diagenetic processes occurred early in the TOCA Fm. burial history, so that the TOCA Fm. acquired its reservoir properties during the first 35 Ma following its deposition. Especially, the current porosity of the TOCA Fm. was acquired during early diagenesis and has not significantly evolved since 95 Ma. Early cementation and chemical compaction by stylolitization followed by reprecipitation of the dissolved material in the residual porosity were quantitatively the main factors controlling the destruction of the reservoir properties in this tight carbonate reservoir.
- U–Pb dating and fluid inclusion microthermometry of calcite cement revealed that the early mineralizing fluids were hot (80–160 °C) highly saline (300–360 g/l) brines, not in thermal equilibrium with the host rocks buried at a maximum depth at 400–500 m at the time of cementation. These hydrothermal fluids likely originated from the pre-rift Precambrian rocks along syn-rift normal faults. These results (combined age and fluid inclusions) illustrate that T_h recorded in the C1 cement cannot be used to infer precipitation depth.

Beyond regional implications, this study demonstrates the potential of our new multi-proxy approach combining stylolite inversion paleopiezometry, fluid inclusion microthermometry, calcite cement U–Pb dating, burial modelling and cement phase petrography image analysis to reconstruct both the timing and amount of porosity destruction in deeply buried tight carbonates reservoirs. In addition, our results illustrate the potential of stylolite roughness inversion to constrain part of the burial history of a carbonate strata, and to grant indirect timing information on the diagenetic evolution of this strata. We show that carbonate texture impacts the overall distribution and development of stylolites, and that considering a given morphology of stylolite, the paleoburial it records seems to be dependent on the texture, being higher in mud-supported rocks. Last but not least, our results also illustrate that the reservoir quality of bioclastic carbonates may be primarily controlled and set as a result of early, very shallow diagenetic processes, leaving only minor potential of impact to the subsequent deep-burial mesogenetic diagenesis.

The original multi-proxy methodology described in this paper is expected to be most useful for application to the reconstruction of diagenetic processes and concomitant porosity evolution in carbonate reservoirs, as shown here. It may also provide valuable information for the calibration of basin models, in particular when dealing with extensively stylolitized carbonates which original thickness may have been significantly reduced by stylolitization.

Declaration of competing interest

The authors declare that they have no known competing financial interests or personal relationships that could have appeared to influence the work reported in this paper.

Data availability

Data will be made available on request.

Acknowledgments

The authors are very grateful to TotalEnergies for complete financial support of this research, for providing the cores and for permission to publish. We would like to thank Philippe Marchina for his help in carrying out the geomechanical tests and for the discussions on the results. Nicolas E. Beaudoin is funded through the isite-E2S, supported by the ANR PIA and the Région Nouvelle-Aquitaine. The laser U–Pb dating analyses were carried out as part of the CEREGE-TotalEnergies collaborative R&D project DATCARB (2018–2021), co-funded by the "Excellence Initiative" program of Aix Marseille University A*MIDEX, TotalEnergies, and Sud region. Abel Guihou is thanked for its technical support in the U–Pb analyses by LA-ICPMS. The authors would also like to thank the editor Bo Liu and three anonymous reviewers for their useful comments and suggestions that improved the quality of the paper.

Appendix A. Supplementary data

Supplementary data to this article can be found online at https://doi.org/10.1016/j.marpetgeo.2022.106018.

References

Aharonov, E., Katsman, R., 2009. Interaction between pressure-solution and clays in stylolite development: insights from modeling. Am. J. Sci. 309 (7), 607–632.
Alvarez, W., Engelder, T., Geiser, P.A., 1978. Classification of solution cleavage in pelagic limestones. Geology 6 (5), 263–266.
Andrews, L.M., Railsback, L.B., 1997. Controls on stylolite development: morphologic, lithologic, and temporal evidence from bedding-parallel and transverse stylolites from the US Appalachians. J. Geol. 105 (1), 59–73.
Aslanian, D., Moulin, M., Olivet, J.L., Unternehr, P., Matias, L., Bache, F., Rabineau, M., Klingelheofer, F., Contrucci, I., Labails, C., 2009. Brazilian and african passive margins of the central segment of the South Atlantic ocean: kinematic constraints. Tectonophysics 468 (1–4), 98–112.
Asmus, H.E., Ponte, F.C., 1973. The Brazilian marginal basins. In: The South Atlantic. Springer, Boston, MA, pp. 87–133.
Bate, R.H., 1999. Non-marine ostracod assemblages of the Pre-Salt rift basins of West Africa and their role in sequence stratigraphy. Geological Society, London, Special Publications 153 (1), 283–292.
Barbier, M., Hamon, Y., Callot, J.P., Floquet, M., Daniel, J.M., 2012. Sedimentary and diagenetic controls on the multiscale fracturing pattern of a carbonate reservoir: the Madison Formation (Sheep Mountain, Wyoming, USA). Mar. Petrol. Geol. 29 (1), 50–67.
Bathurst, R.G., 1972. Carbonate Sediments and Their Diagenesis. Elsevier, pp. 459–475.
Baud, P., Rolland, A., Heap, M., Xu, T., Nicolé, M., Ferrand, T., Reuschlé, T., Toussaint, R., Conil, N., 2016. Impact of stylolites on the mechanical strength of limestone. Tectonophysics 690, 4–20.
Baudino, R., Pontet, M., Manas, M., Herra, A., Sanders, C., Badali, M., Tocco, R., Martinez, S., Tritlla, J., Loma, R., Carrasco, A., Padron, S., Mora, S., 2018. Modelling petroleum systems of hyperextended margins: the Angola case study. In: Global Analogues for the Atlantic Margin. AAPG European Regional Conference, Abstracts.
Beaudoin, N., Lacombe, O., Koehn, D., David, M.E., Farrell, N., Healy, D., 2020a. Vertical stress history and paleoburial in foreland basins unravelled by stylolite roughness paleopiezometry: insights from bedding-parallel stylolites in the Bighorn Basin, Wyoming, USA. J. Struct. Geol. 136, 104061.
Beaudoin, N., Lacombe, O., David, M.E., Koehn, D., 2020b. Does stress transmission in forelands depend on structural style? Distinctive stress magnitudes during Sevier thin-skinned and Laramide thick-skinned layer-parallel shortening in the Bighorn Basin (USA) revealed by stylolite and calcite twinning paleopiezometry. Terra. Nova 32 (3), 225–233.
Beaudoin, N.E., Labeur, A., Lacombe, O., Koehn, D., Billi, A., Hoareau, G., Boyce, A., John, C.M., Marchegiano, M., Robert, N.M., Millar, I.L., Clavery, F., Pecheyran, C., Callot, J.P., 2020c. Regional-scale paleofluid system across the Tuscan Nappe–Umbria–Marche Apennine Ridge (northern Apennines) as revealed by mesostructural and isotopic analyses of stylolite–vein networks. Solid Earth 11 (4), 1617–1641.
Beaudoin, N., Gasparrini, M., David, M.E., Lacombe, O., Koehn, D., 2019. Bedding-parallel stylolites as a tool to unravel maximum burial depth in sedimentary basins: application to Middle Jurassic carbonate reservoirs in the Paris basin. Geol. Soc. Am. Bull. 131 (7/8), 1239–1254.
Beaudoin, N., Lacombe, O., Roberts, N.M., Koehn, D., 2018. U-Pb dating of calcite veins reveals complex stress evolution and thrust sequence in the Bighorn Basin, Wyoming, USA. Geology 46 (11), 1015–1018.
Beaudoin, N., Lacombe, O., 2018. Recent and future trends in paleopiezometry in the diagenetic domain: insights into the tectonic paleostress and burial depth history of fold-and-thrust belts and sedimentary basins. J. Struct. Geol. 114, 357–365.
Beaudoin, N., Koehn, D., Lacombe, O., Lecouty, A., Billi, A., Aharonov, E., Parlangeau, C., 2016. Fingerprinting stress: stylolite and calcite twinning paleopiezometry revealing the complexity of progressive stress patterns during

folding—the case of the Monte Nero anticline in the Apennines, Italy. Tectonics 35 (7), 1687–1712.
Bebout, D.G., 1974. Stuart City Trend, Lower Cretaceous, South Texas: a Carbonate Shelf-Margin Model for Hydrocarbon Exploration. Virtual Landscapes of Texas.
Beglinger, S.E., Doust, H., Cloetingh, S., 2012. Relating petroleum system and play development to basin evolution: west African South Atlantic basins. Mar. Petrol. Geol. 30 (1), 1–25.
Ben-Itzhak, L.L., Aharonov, E., Karcz, Z., Kaduri, M., Toussaint, R., 2014. Sedimentary stylolite networks and connectivity in limestone: large-scale field observations and implications for structure evolution. J. Struct. Geol. 63, 106–123.
Bertotti, G., de Graaf, S., Bisdom, K., Oskam, B., Vonhof, H.B., Bezerra, F.H.R., Reijmer, J.J.G., Cazarin, C.L., 2017. Fracturing and fluid-flow during post-rift subsidence in carbonates of the jandaíra formation, potiguar basin, NE Brazil. Basin Res. 29 (6), 836–853.
Bidiet, J., Kinga, A., Loemba, C., Assoua-Wande, C., Hossie, G., Mahoukou-Sounga, A., 1998. Aperçu géologique et pétrolier des bassins du congo. Rapport de l'association des producteurs de pétrole africains, Hydro-Congo, Elf-Congo, AGIP Congo. Ministère des Mines et de l'Energie, p. RF11904.
Booler, J., Tucker, M.E., 2002. Distribution and geometry of texture and early diagenesis: the key to accommodation space variation and sequence stratigraphy: upper Cretaceous Congost Carbonate platform, Spanish Pyrenees. Sediment. Geol. 146 (3–4), 225–247.
Brice, S.E., Cochran, M.D., Pardo, G., Edwards, A.D., 1982. Tectonics and sedimentation of the South Atlantic Rift Sequence: Cabinda, Angola: rifted margins: field investigations of margin structure and stratigraphy. In: Studies in Continental Margin Geology. AAPG Special Volumes, pp. 5–18.
Brognon, G.P., Verrier, G.R., 1966. Oil and geology in cuanza basin of Angola. AAPG (Am. Assoc. Pet. Geol.) Bull. 50 (1), 108–158.
Brownfield, M.E., Charpentier, R.R., 2006. Geology and Total Petroleum Systems of the West-Central Coastal Province (7203), West Africa (No. 2207-B). US Geological Survey.
Bruna, P.O., Lavenu, A.P., Matonti, C., Bertotti, G., 2019. Are stylolites fluid-flow efficient features? J. Struct. Geol. 125, 270–277.
Burk, K., Dewey, J.F., 1974. Two plates in Africa during the cretaceous? Nature 249 (5455), 313–316.
Burwood, R., 1999. Angola: source rock control for Lower Congo Coastal and Kwanza Basin petroleum systems. Geological Society, London, Special Publications 153 (1), 181–194.
Bushinskiy, G.I., 1961. Stylolites. Izv. Akad. Nauk. SSSR, Ser. Fiz 8, 31–46.
Buxton, T.M., Sibley, D.F., 1981. Pressure-solution features in a shallow buried limestone. J. Sediment. Res. 51 (1), 19–26.
Carozzi, A.V., Bergen, D.V., 1987. Stylolitic porosity in carbonates: a critical factor for deep hydrocarbon production. J. Petrol. Geol. 10 (3), 267–282.
Chaboureau, A.C., Guillocheau, F., Robin, C., Rohais, S., Moulin, M., Aslanian, D., 2013. Paleogeographic evolution of the central segment of the South Atlantic during Early Cretaceous times: paleotopographic and geodynamic implications. Tectonophysics 604, 191–223.
Choquette, P.W., Pray, L.C., 1970. Geologic nomenclature and classification of porosity in sedimentary carbonates. AAPG Bull. 54 (2), 207–250.
Contrucci, I., Matias, L., Moulin, M., Géli, L., Klingelhofer, F., Nouzé, H., Aslanian, D., Olivet, J.L., Réhault, J.P., Sibuet, J.C., 2004. Deep structure of the West African continental margin (Congo, Zaïre, Angola), between 5 S and 8 S, from reflection/refraction seismics and gravity data. Geophys. J. Int. 158 (2), 529–553.
Croize, D., Renard, F., Gratier, J.P., 2013. Compaction and porosity reduction in carbonates: a review of observations, theory, and experiments. Adv. Geophys. 54, 181–238.
Da Costa, J.L., Schirmer, T.W., Laws, B.R., 1999. Lower Congo basin, deepwater exploration province. offshore West Afri~ AAPG Bulletin 83 (12).
Delpomdor, F., Préat, A., Tack, L., 2008. Paleoenvironments of the neoproterozoic carbonates in the schisto-calcaire Subgroup (C2 and C3) in democratic republic of Congo: lithostratigraphy and diagenesis. In: 22nd Colloquium of African Geology (CAG22) & 13th Conference of the. Geological Society of Africa (GSAf13) (109).
Desthieux, F., 1993. Notice explicative de la carte géologique de la République du Congo au 1/1.000. 000. Ministère des mines et de l'énergie, vol. 27. Direction Générale des Mines. Brazzaville.
Dingle, R.V., 1999. Walvis Ridge barrier: its influence on palaeoenvironments and source rock generation deduced from ostracod distributions in the early South Atlantic Ocean. Geological Society, London, Special Publications 153 (1), 293–302.
Doyle, J.A., Jardiné, S., Doerenkamp, A., 1982. Afropolis, un nouveau genre de pollen d'Angiosperme précoce, avec de données sur la palynostratigraphie et les paléoenvironnements du Crétacé du Nord-Gondwana. Bulletin des Centres de Recherche et d'Exploration-Production Elf-Aquitaine 6, 39–117.
Dunnington, H.V., 1954. Stylolite development post-dates rock induration. J. Sediment. Res. 24 (1), 27–49.
Ebner, M., Piazolo, S., Renard, F., Koehn, D., 2010a. Stylolite interfaces and surrounding matrix material: nature and role of heterogeneities in roughness and microstructural development. J. Struct. Geol. 32 (8), 1070–1084.
Ebner, M., Toussaint, R., Schmittbuhl, J., Koehn, D., Bons, P., 2010b. Anisotropic scaling of tectonic stylolites: a fossilized signature of the stress field? J. Geophys. Res. Solid Earth 115 (B6).
Ebner, M., Koehn, D., Toussaint, R., Renard, F., 2009a. The influence of rock heterogeneity on the scaling properties of simulated and natural stylolites. J. Struct. Geol. 31 (1), 72–82.
Ebner, M., Koehn, D., Toussaint, R., Renard, F., Schmittbuhl, J., 2009b. Stress sensitivity of stylolite morphology. Earth Planet Sci. Lett. 277 (3–4), 394–398.
Ehrenberg, S.N., Morad, S., Yaxin, L., Chen, R., 2016. Stylolites and porosity in a lower cretaceous limestone reservoir, onshore abu dhabi, UAE. J. Sediment. Res. 86 (10), 1228–1247.
Ehrenberg, S.N., Nadeau, P.H., Steen, Ø., 2009. Petroleum reservoir porosity versus depth: influence of geological age. AAPG Bull. 93 (10), 1281–1296.
Ehrenberg, S.N., Nadeau, P.H., 2005. Sandstone vs. carbonate petroleum reservoirs: a global perspective on porosity-depth and porosity-permeability relationships. AAPG Bull. 89 (4), 435–445.
Giresse, P., 1982. La succession des sédiments dans les bassins marins et continentaux du Congo depuis le début du Mésozoïque. Sciences Géologiques, bulletins et mémoires 35 (4), 183–206.
Godeau, N., Deschamps, P., Guihou, A., Leonide, P., Tendil, A., Gerdes, A., Hamelin, B., Girard, J.P., 2018. U-Pb dating of calcite cement and diagenetic history in microporous carbonate reservoirs: case of the Urgonian Limestone. France. Geology 46 (3), 247–250.
Goldstein, R.H., Reynolds, T.J., 1994. Systematics of Fluid Inclusions in Diagenetic Minerals. SEPM Short Course No. 31. SEPM Society for Sedimentary Geology.
Gomez-Rivas, E., Martín-Martín, J.D., Bons, P.D., Koehn, D., Griera, A., Travé, A., Llorens, M.G., Humphrey, E., Neilson, J., 2022. Stylolites and stylolite networks as primary controls on the geometry and distribution of carbonate diagenetic alterations. Mar. Petrol. Geol. 136, 105444.
Gradstein, F.M., Ogg, J.G., Smith, A.G., Bleeker, W., Lourens, L.J., 2004. A new geologic time scale, with special reference to Precambrian and Neogene. Episodes 27 (2), 83–100.
Grosdidier, E., Braccini, E., Dupont, G., Moron, J.M., 1996. Biozonation du Crétacé Inférieur non marin des bassins du Gabon et du Congo. Bulletin des Centres de recherches exploration-production Elf-Aquitaine. Memoir (16), 67–82.
Grosdidier, E., 1967. Quelques ostracodes nouveaux de la Série anté–salifère ("Wealdienne") des bassins côtiers du Gabon et du Congo. Rev. Micropaleontol. 10 (2), 107–118.
Guillocheau, F., Chelalou, R., Linol, B., Dauteuil, O., Robin, C., Mvondo, F., Callec, Y., Colin, J.P., 2015. Cenozoic landscape evolution in and around the Congo Basin: constraints from sediments and planation surfaces. In: Geology and Resource Potential of the Congo Basin. Springer, Berlin, Heidelberg, pp. 271–313.
Guiraud, M., Buta-Neto, A., Quesne, D., 2010. Segmentation and differential post-rift uplift at the Angola margin as recorded by the transform-rifted Benguela and oblique-to-orthogonal-rifted Kwanza basins. Mar. Petrol. Geol. 27 (5), 1040–1068.
Guiraud, R., Maurin, J.C., 1991. Le Rifting en Afrique au Cretace inferieur; synthese structurale, mise en evidence de deux etapes dans la genese des bassins, relations avec les ouvertures oceaniques peri-africaines. Bull. Soc. Geol. Fr. 162 (5), 811–823.
Guo, X., Dong, F., Du, Z., 2006. Design and demonstration of creating underground gas storage in a fractured oil depleted carbonate reservoir. In: SPE Russian Oil and Gas Technical Conference and Exhibition. OnePetro.
Harris, N.B., 2000. Toca Carbonate, Congo Basin: response to an evolving rift lake. In: Mello, M.R., Katz, B.J. (Eds.), Petroleum systems of South Atlantic margins: AAPG Memoir 73, pp. 341–360.
Heap, M., Reuschlé, T., Baud, P., Renard, F., Iezzi, G., 2018. The permeability of stylolite-bearing limestone. J. Struct. Geol. 116, 81–93.
Harris, N.B., Sorriaux, P., Toomey, D.F., 1994. Geology of the Lower Cretaceous Viodo Carbonate, Congo Basin: a lacustrine carbonate in the South Atlantic rift. in A. J. Lomando, B. C. Schreiber, and P. M. Harris, eds., Lacustrine reservoirs and depositional systems: SEPM Core Workshop No. 19, 143–172.
Heap, M.J., Baud, P., Reuschlé, T., Meredith, P.G., 2014. Stylolites in limestones: barriers to fluid flow? Geology 42 (1), 51–54.
Hintze, J.L., Nelson, R.D., 1998. Violin plots: a box plot-density trace synergism. Am. Statistician 52 (2), 181–184.
Humphrey, E., Gomez-Rivas, E., Koehn, D., Bons, P.D., Neilson, J., Martín-Martín, J.D., Schoenherr, J., 2019. Stylolite-controlled diagenesis of a mudstone carbonate reservoir: a case study from the Zechstein 2 Carbonate (Central European Basin, NW Germany). Mar. Petrol. Geol. 109, 88–107.
Kadima, E., Delvaux, D., Sebagenzi, S.N., Tack, L., Kabeya, S.M., 2011. Structure and geological history of the Congo Basin: an integrated interpretation of gravity, magnetic and reflection seismic data. Basin Res. 23 (5), 499–527.
Karner, G.D., Gambôa, L.A.P., 2007. Timing and origin of the South Atlantic pre-salt sag basins and their capping evaporites. Geological Society, London, Special Publications 285 (1), 15–35.
Karner, G.D., Driscoll, N.W., Barker, D.H.N., 2003. Syn-rift regional subsidence across the West African continental margin: the role of lower plate ductile extension. Geological Society, London, Special Publications 207 (1), 105–129.
Karner, G.D., Driscoll, N.W., 1999. Tectonic and stratigraphic development of the West African and eastern Brazilian Margins: insights from quantitative basin modelling. Geological Society, London, Special Publications 153 (1), 11–40.
Koehn, D., Koehler, S., Toussaint, R., Ghani, I., Stollhofen, H., 2022. Scaling analysis, correlation length and compaction estimates of natural and simulated stylolites. J. Struct. Geol., 104670
Koehn, D., Rood, M.P., Beaudoin, N., Chung, P., Bons, P.D., Gomez-Rivas, E., 2016. A new stylolite classification scheme to estimate compaction and local permeability variations. Sediment. Geol. 346, 60–71.
Koehn, D., Ebner, M., Renard, F., Toussaint, R., Passchier, C.W., 2012. Modelling of stylolite geometries and stress scaling. Earth Planet Sci. Lett. 341, 104–113.
Koehn, D., Renard, F., Toussaint, R., Passchier, C.W., 2007. Growth of stylolite teeth patterns depending on normal stress and finite compaction. Earth Planet Sci. Lett. 257 (3–4), 582–595.
Labeur, A., Beaudoin, N.E., Lacombe, O., Emmanuel, L., Petracchini, L., Daëron, M., Klimowicz, S., Callot, J.P., 2021. Burial-deformation history of folded rocks unraveled by fracture analysis, stylolite paleopiezometry and vein cement

geochemistry: a case study in the Cingoli Anticline (Umbria-Marche, Northern Apennines). Geosciences 11 (3), 135.
Lacombe, O., Beaudoin, N.E., Hoareau, G., Labeur, A., Pecheyran, C., Callot, J.P., 2021. Dating folding beyond folding, from layer-parallel shortening to fold tightening, using mesostructures: lessons from the Apennines, Pyrenees, and Rocky Mountains. Solid Earth 12 (10), 2145–2157.
Lehner, P., De Ruiter, P.A.C., 1977. Structural history of the atlantic margin of Africa. AAPG (Am. Assoc. Pet. Geol.) Bull. 61 (7), 961–981.
Li, Q., Parrish, R.R., Horstwood, M.S.A., McArthur, J.M., 2014. U–Pb dating of cements in Mesozoic ammonites. Chem. Geol. 376, 76–83.
Macgregor, D.S., 2020. Regional variations in geothermal gradient and heat flow across the African plate. J. Afr. Earth Sci. 171, 103950.
Martin-Martin, J.D., Gomez-Rivas, E., Gomez-Gras, D., Travé, A., Ameneiro, R., Koehn, D., Bons, P.D., 2018. Activation of stylolites as conduits for overpressured fluid flow in dolomitized platform carbonates. Geological Society, London, Special Publications 459 (1), 157–176.
Masson, M.P., 1972. L'exploration pétrolière en Angola. Revue de l'Association Française des Techniciens du Pétrole, p. 212.
Matton, G., Jébrak, M., 2009. The Cretaceous Peri-Atlantic Alkaline Pulse (PAAP): deep mantle plume origin or shallow lithospheric break-up? Tectonophysics 469 (1–4), 1–12.
Mbina Mounguengui, M., Guiraud, M., 2009. Neocomian to early aptian syn-rift evolution of the normal to oblique-rifted north Gabon margin (interior and n'komi basins). Mar. Petrol. Geol. 26 (6), 1000–1017.
McHargue, T.R., 1990. Stratigraphic Development of Proto-South Atlantic Rifting in Cabinda, Angola–A Petroliferous Lake Basin (Chapter 19).
Mohriak, W., Nemčok, M., Enciso, G., 2008. South Atlantic divergent margin evolution: rift-border uplift and salt tectonics in the basins of SE Brazil. Geological Society, London, Special Publications 294 (1), 365–398.
Mohriak, W.U., 2003. Sedimentary basins of the Brazilian continental margin. In: Bizzi, L.A., Schobbenhaus, C., Vidotti, R.M., Goncalves, J.H. (Eds.), Geologia, Tectonica e Recursos Minerais do Brasil. CPRM, Brasilia, pp. 87–165 (Chapter 3).
Moore, C.H., Wade, W.J., 2013. Carbonate Reservoirs: Porosity and Diagenesis in a Sequence Stratigraphic Framework. Newnes, pp. 3–20.
Moore, C.H., 1989. Carbonate Diagenesis and Porosity. Elsevier, pp. 43–71.
Moulin, M., Aslanian, D., Unternehr, P., 2010. A new starting point for the South and equatorial Atlantic Ocean. Earth Sci. Rev. 98 (1–2), 1–37.
Moulin, M., Aslanian, D., Olivet, J.L., Contrucci, I., Matias, L., Géli, L., Klingelhoefer, F., Nouzé, H., Unternehr, P., 2005. Geological constraints on the evolution of the Angolan margin based on reflection and refraction seismic data (ZaïAngo project). Geophys. J. Int. 162 (3), 793–810.
Mussard, J.M., 1996. Les palynomorphes, indicateurs des variations du niveau marin relatif: analyses quantitatives dans l'Albien supérieur de la République du Congo. In: Jardiné, S., de Klasz, I., Debenay, J.-P. (Eds.), Géologie de l'Afrique et de l'Atlantique Sud, Compte Rendus des Colloques de géologie d'Angers, 16–24 juillet 1994, Mémoires du Bulletin des Centres de Recherche et d'Exploration-Production d'Elf, vol. 16, pp. 57–66, 1996.
Park, W.C., Schot, E.H., 1968. Stylolites; their nature and origin. J. Sediment. Res. 38 (1), 175–191.
Perrier, R., Quiblier, J., 1974. Thickness changes in sedimentary layers during compaction history; methods for quantitative evaluation. AAPG Bull. 58 (3), 507–520.
Pletsch, T., Erbacher, J., Holbourn, A.E., Kuhnt, W., Moullade, M., Oboh-Ikuenobede, F. E., Söding, E., Wagner, T., 2001. Cretaceous separation of Africa and south America: the view from the West African margin (ODP leg 159). J. S. Am. Earth Sci. 14 (2), 147–174.
Préat, A., Kolo, K., Prian, J.P., Delpomdor, F., 2010. A peritidal evaporite environment in the neoproterozoic of south Gabon (Schisto-Calcaire Subgroup, nyanga basin). Precambrian Res. 177 (3–4), 253–265.
Railsback, L.B., 1993. Lithologic controls on morphology of pressure-dissolution surfaces (stylolites and dissolution seams) in Paleozoic carbonate rocks from the mideastern United States. J. Sediment. Res. 63 (3), 513–522.
Regnet, J.B., David, C., Robion, P., Menéndez, B., 2019. Microstructures and physical properties in carbonate rocks: a comprehensive review. Mar. Petrol. Geol. 103, 366–376.
Renard, F., Schmittbuhl, J., Gratier, J.P., Meakin, P., Merino, E., 2004. Three-dimensional roughness of stylolites in limestones. J. Geophys. Res. Solid Earth 109 (B3).
Renard, F., Ortoleva, P., Gratier, J.P., 1997. Pressure solution in sandstones: influence of clays and dependence on temperature and stress. Tectonophysics 280 (3–4), 257–266.
Robert, P., Yapaudjian, L., 1990. Early Cretaceous rift sediments of the Gabon-Congo margin: lithology and organic matter; tectonic and paleogeothermal evolution. J. Afr. Earth Sci. 10 (1–2), 319–330.
Roberts, N.M., Lee, J.K., Holdsworth, R.E., Jeans, C., Farrant, A.R., Haslam, R., 2020. Near-surface Palaeocene fluid flow, mineralisation and faulting at Flamborough Head, UK: new field observations and U–Pb calcite dating constraints. Solid Earth 11 (5), 1931–1945.
Roberts, N.M., Rasbury, E.T., Parrish, R.R., Smith, C.J., Horstwood, M.S., Condon, D.J., 2017. A calcite reference material for LA-ICP-MS U-Pb geochronology. G-cubed 18 (7), 2807–2814.
Roedder, E., 1984. Volume 12: fluid inclusions. Rev. Mineral. 12.
Rolland, A., Toussaint, R., Baud, P., Conil, N., Landrein, P., 2014. Morphological analysis of stylolites for paleostress estimation in limestones. Int. J. Rock Mech. Min. Sci. 67, 212–225.
Rolland, A., Toussaint, R., Baud, P., Schmittbuhl, J., Conil, N., Koehn, D., Renard, F., Gratier, J.P., 2012. Modeling the Growth of Stylolites in Sedimentary.
Salem, A.M., Shedid, S.A., 2013. Variation of petrophysical properties due to carbon dioxide (CO2) storage in carbonate reservoirs. J. Petrol. Gas Eng. 4 (4), 91–102.
Schmittbuhl, J., Renard, F., Gratier, J.P., Toussaint, R., 2004. Roughness of stylolites: implications of 3D high resolution topography measurements. Phys. Rev. Lett. 93 (23), 238501.
Schmoker, J.W., Halley, R.B., 1982. Carbonate porosity versus depth: a predictable relation for south Florida. AAPG (Am. Assoc. Pet. Geol.) Bull. 66 (12), 2561–2570, 9.
Schoellkopf, N.B., Patterson, B.A., 2000. AAPG Memoir 73, (Chapter 25): Petroleum Systems of Offshore Cabinda (Angola).
Scholle, P.A., 1977. Chalk diagenesis and its relation to petroleum exploration: oil from chalks, a modern miracle? AAPG (Am. Assoc. Pet. Geol.) Bull. 61 (7), 982–1009.
Schroeder, J.H., 1988. Spatial variations in the porosity development of carbonate sediments and rocks. Texture 18 (1), 181–204.
Séranne, M., Anka, Z., 2005. South Atlantic continental margins of Africa: a comparison of the tectonic vs climate interplay on the evolution of equatorial west Africa and SW Africa margins. J. Afr. Earth Sci. 43 (1–3), 283–300.
Stockdale, P.B., 1943. Stylolites, primary or secondary? J. Sediment. Res. 13 (1), 3–12.
Stockdale, P.B., 1936. Rare stylolites. Am. J. Sci. 5 (188), 129–133.
Stockdale, P.B., 1926. The stratigraphic significance of solution in rocks. J. Geol. 34 (5), 399–414.
Stockdale, P.B., 1922. Stylolites: their nature and origin. Indiana Univ. Stud. 9 (55), 1–97.
Szatmari, P., Milani, E.J., 2016. Tectonic control of the oil-rich large igneous-carbonate-salt province of the South Atlantic rift. Mar. Petrol. Geol. 77, 567–596.
Teisserenc, P., Villemin, J., 1989. Sedimentary basin of Gabon–geology and oil systems. In: Edwards, J.D., Santogrossi, P.A. (Eds.), Divergent/passive Margins Basins, vol. 48. AAPG, pp. 117–199, 1990.
Torsvik, T.H., Rousse, S., Labails, C., Smethurst, M.A., 2009. A new scheme for the opening of the South Atlantic Ocean and the dissection of an Aptian salt basin. Geophys. J. Int. 177 (3), 1315–1333.
Toussaint, R., Aharonov, E., Koehn, D., Gratier, J.P., Ebner, M., Baud, P., Rolland, A., Renard, F., 2018. Stylolites: a review. J. Struct. Geol. 114, 163–195.
Tucker, M., 2001. Carbonate reservoirs: porosity evolution and diagenesis in sequence stratigraphic framework-by clyde Moore, published by elsevier, amsterdam, developments in sedimentology volume 55, 2001, 444. Org. Geochem. 11 (32), 1373.
Tucker, M.E., Wright, V.P., 1990. Diagenetic processes, products and environments. Carbonate sedimentology 314, 364.
Uncini, G., Brandao, M., Giovannelli, A., 1998. In: ABGP/AAPG International Conference and Exhibition November 8-11, 1998. Neocomian-Upper Aptian Pre-Salt sequence of southern Kwanza Basin: a regional view, Rio de Janeiro, Brazil.
Vandeginste, V., John, C.M., 2013. Diagenetic implications of stylolitization in pelagic carbonates, Canterbury Basin, offshore New Zealand. J. Sediment. Res. 83, 226–240.
Vernet, R., Assoua-Wande, C., Massamba, L., Sorriaux, P., 1996. Paléogéographie du Crétacé (Albien-Maastrichtien) du bassin côtier congolais. Bull. Cent. Rech. Explor.-Prod. Elf-Aquitaine - Mem. (16), 39–55.
Wang, L., He, Y., Peng, X., Deng, H., Liu, Y., Xu, W., 2020. Pore structure characteristics of an ultradeep carbonate gas reservoir and their effects on gas storage and percolation capacities in the Deng IV member, Gaoshiti-Moxi Area, Sichuan Basin, SW China. Mar. Petrol. Geol. 111, 44–65.
Woodhead, J.D., Hergt, J.M., 2001. Strontium, neodymium and lead isotope analyses of NIST glass certified reference materials: srm 610, 612, 614. Geostand. Newsl. 25 (2–3), 261–266.
Wright, K., Cygan, R.T., Slater, B., 2001. Structure of the (1014) surfaces of calcite, dolomite and magnesite under wet and dry conditions. Phys. Chem. Chem. Phys. 3 (5), 839–844.
Xu, J., Deng, Y., Fu, M., Guo, R., Chen, P., Duan, G., Ma, R., 2022. The nonuniform distribution of stylolite in bioclastic limestones and its influence on reservoir petrophysical properties—a case study of the mishrif formation from the ah oilfield. Energies 15 (9), 3032.